DOI: 10.1016/j.pss.2022.105451

Planetary and Space Science 214 (2022) 105451

On the stability and phase behavior of Titan's subsurface liquid columns

Sugata P. Tan[1*], Hertanto Adidharma[2]

[1]Planetary Science Institute, Tucson, AZ 85719, USA

[2]Depatment of Petroleum Engineering, University of Wyoming, Laramie WY 82071, USA

ABSTRACT

On Titan, liquid hydrocarbon may stay in the subsurface porous permeable crust known as the alkanofer, analogous to water in Earth's aquifer. In addition to pressure gradient, the subsurface liquid in alkanofers is subject to vertical compositional grading due to the gravity and temperature gradient. The common wisdom is that the liquid would normally stay underground in a stability established by the pressure that increases with depth as observed in aquifers on Earth. However, Titan's liquids consist of nitrogen and hydrocarbons, mainly methane and ethane, the behavior of which is very sensitive to temperature and pressure. Consequently, the liquid density does not always increase with depth, thus may introduce a reverse density profile that leads to vertical convective instability of the liquid column. If reverse density profiles are present, capillary pressures arising from liquid trapped within small pores in the crust can help with the column stability. The liquid held in the capillaries can seal the space below it thus helping with the stability, unless the overpressure built from underneath becomes larger than the capillary pressure, which causes leakage to allow the liquids to seep upward from the deep. This situation is analogous to hydrocarbon seeps on Earth, where oil and natural gas escape the reservoir and flow slowly through network of cracks to the surface. An algorithm based on an extended Gibbs equa-

---

[*] Corresponding author: stan@psi.edu

tion commonly used in petroleum reservoir engineering is employed in this work to produce pressure, density, and compositional profiles for evaluating the stability and phase behavior of Titan’s subsurface fluids.

KEYWORDS: Titan; subsurface liquid; alkanofer; thermo-gravitational effects; capillary pressure

1. Introduction

In gravitational fields, any fluid mixtures will experience the hydrostatic effect and compositional grading with depth, which provide vertical compositional gradient with a tendency of heavy components migrating to greater depths. In the meantime, the temperature gradient due to geothermal activities introduces an opposing effect to the composition, because the lighter components also tend to go deeper through diffusion as the temperature increases. These thermo-gravitational effects are very important, e.g., in oil-gas recovery from reservoirs on Earth (Høier & Whitson, 2000; Galliero et al., 2016), where the composition of hydrocarbon at the well bore is different from the composition in the reservoir.

Similar situations would likely occur in the subsurface alkanofer on Titan (Vance et al., 2012; Mousis et al., 2014) where the hydrocarbon liquids may attain high hydrostatic pressures due to the depth, as well as higher temperatures due to the temperature gradient. The subsurface alkanology, analogous to terrestrial hydrology, may exist with water-ice upper crust that is thermally conductive and likely porous and has fractures to allow subsurface liquid flow. Methane-based hydrological cycle on Titan is discussed in a comprehensive review paper (Hayes et al., 2018). The topmost layer of the crust may also be covered by methane clathrate of several kilometers thick that increases the temperature gradient below it due to its lower heat conductivity than water ice (Kalousova & Sotin, 2020). The existence of clathrate crust could in fact be the most realistic crust environment on Titan due to the presence of hydrocarbon.

While the hydrostatic pressure on Earth is easily calculated for water based on its density behavior with temperature and pressure, it is not the case with Titan’s liquid, which is a mixture of nitrogen and hydrocarbons (Tan et al., 2013; 2015) – mainly methane and ethane (Brown et al., 2008; Mastrogiuseppe et al. 2015; Tan & Kargel, 2018). On the surface, the liquid is in equilibrium with the atmosphere at conditions observed by Huygens probe. At this equilibrium, the density of the mixture, thus also the composition, is sensitive to pressure and temperature in a counter-intuitive way, where it can become denser with temperature and lighter with pressure (Tan et al., 2015).

Recent treatments have simultaneously applied both gravitational and thermal diffusion to obtain the compositional grading so that the subsurface conditions, including the pressure gradient, can be calculated more realistically for Titan’s alkanofers (Tan & Kargel, 2020; Cordier et al., 2021). The treatments assume that the subsurface liquid column has reached a steady state, so that stationary compositional gradients can be obtained. In fact, this is generally true for hydrocarbon reservoir on Earth, where the liquid column is stable as the vertical convective flow is practically absent (England et al., 1987). As this work will show later, it is not always the case for Titan’s subsurface liquids, of which the density profile can be reversed, i.e., the density decreases with depth. This reverse density profile leads to convection, thus unstable system (Galliero et al., 2016). Therefore, it is very critical to evaluate the stability of liquid columns on Titan, which is usually taken for granted despite its importance for more realistic conditions of the subsurface liquids.

As happens on Earth, subsurface liquids, both water and hydrocarbons, may also be stored inside small pores underground. Liquids trapped in pores have strong interaction with the pore wall, known as capillary pressure, which hold the liquids from expulsion (Berg, 1975). Only if there is a sufficient pressure difference across the ends of the pores, the capillary pressure is overcome to release the liquids out from the pores. Therefore, a layer of crust with small pores can entrap liquids and withstand pressure difference that is less than the existing capillary pressure to block any possible flow across the layer (England et al., 1987). These filled capillaries effectively seal the space below them, such as that in aquitard or caprock on Earth sealing oil reservoirs at the top, and thus stabilize the liquid columns, e.g., from vertical convective flow as mentioned earlier. Such a layer may be called as alkanotard on Titan as the liquid contains mostly alkanes, i.e., methane and ethane in this work. The capillary pressure is stronger in smaller pores, thus deeper location due to compaction. Though the exact magnitude of the capillary pressure that helps the column stability is not possible to obtain, even on Earth due to a vast number of factors, the order of magnitude can be estimated using a state-of-the-art approach applied in this work. Capillary uptake into crust with nanometer-size pores on Titan was first studied using conventional Kelvin's equation (Voss et al., 2007), which treats the vapor phase as an ideal gas and the liquid phase is assumed to be incompressible, both of which are not valid for Titan's fluids as explained later. Moreover, the capillary pressure was not discussed in that paper.

In this work, several cases with thermo-gravitational effects are considered for Titan's subsurface liquids, which are adequately modeled as ternary mixtures of nitrogen, methane, and ethane (Tan & Kargel, 2018). For a single fluid phase, liquid in this case, the thermo-gravitational effects are readily calculated using a simple algorithm (Galliero et al., 2017) as done before (Tan & Kargel, 2020). The algorithm allows us to simultaneously obtain pressure and compositional gradients, and consequently the density profile, for a liquid mixture subject to gravity and a temperature gradient in convection-free conditions. For the record, the subroutine applying this algorithm is not specific to a certain equation of state (EOS), so that any EOS can be used with it to do the calculations if the inputs required by the subroutine are provided. We use PC-SAFT EOS (Gross & Sadowski, 2001), which is accurate in describing fluid phases of mixtures, to be coupled with the subroutines for our investigation. A similar thermo-gravitational treatment has been done with this ternary mixture by Cordier et al. (2021), in which the same

EOS was used but with a different binary parameter, as well as different thermo-diffusion approach, compositions on the surface, and crust environments. Nevertheless, as shown later, our work applies better binary parameter, thermo-diffusion approach, and surface compositions at low- and high-latitude regions, for water-ice and methane-clathrate crusts. Importantly, we investigate the stability of the subsurface liquids, which has never been done before. The stability analysis, as also shown later, is based on the density profile.

Upon evaluation on the vertical stability of liquid columns under various temperature gradients, which are given in Appendix A, the corresponding profiles of capillary pressure will also be determined with respect to depth. This way, when a reverse density profile is present, the magnitude of capillary pressure at the depth of interest that helps with the stability can also be estimated. Note that the evaluation in this work is only based on thermodynamic steady states, so that any implications leading to temporal variations and fluid dynamics in the liquid columns and changes of properties in the crust are not considered, thus open for further investigations.

This paper starts with revisiting the analogy between alkanofers on Titan with aquifers on Earth, which discloses some differences to be cautioned. The methods of thermo-gravity and capillary-pressure calculations are then briefly discussed, followed by the results and discussion. The paper ends with conclusions and remarks as well as appendices that include the algorithms of the thermo-gravitational effects. A supplementary material is also given to accompany the paper in presenting the numerical results plotted in the figures as well as the subroutines coded in FORTRAN for the thermo-gravitational effects.

2. Analogy: Titan’s alkanofers and Earth’s aquifers

It may be beneficial to consider the analogy between alkanofers on Titan with aquifers on Earth in more details, which can be summarized and illustrated in Fig. 1. On Earth, starting from the surface, the atmospheric air may penetrate the vadose zone where liquid does not occupy the whole space. In this zone the pressure is the same as the atmospheric pressure down to the so-called water table, which usually has a profile roughly following the surface curvature except in open liquid bodies such as lakes where the profile is horizontally flat. On Titan, it would be called the alkane table, just to borrow the term from Earth's case. Below the table, there is an unconfined aquifer, or unconfined alkanofer on Titan, where the hydrostatic pressure takes place in constant communication with the atmosphere through the vadose zone. Therefore, the highest level that can be reached by liquids in this layer is the table. At the bottom of the unconfined aquifer, there is an aquitard, i.e., a layer barely permeable to water (Freeze & Cherry, 1975), which may trap another deeper aquifer in the so-called confined aquifer. By analogy, an equivalent alkanotard may be assumed to exist on Titan. In the confined zone, the liquid has both hydrostatic and lithospheric pressures. The latter may be caused by the full weight of the overlying crust materials or just a part of the weight due to partial support from the crustal structure. This lithospheric pressure can send the liquid from the confined aquifer to some height in the air, e.g., in an artesian well. Finally, the confined zone sits on another aquitard, or alkanotard on Titan, which seals the bedrock that may still contain some liquids.

While in many aspects the analogy seems to be comprehensive by substituting liquid water with alkane-rich liquids, as well as the silicate-rich crust with water-ice crust, there are important differences outlined below. On Earth, we may have another fluid in addition to water, which is the hydrocarbons that we call oil and natural gas, so that we often encounter three-phase fluid system underground near hydrocarbon reservoirs. They are aqueous phase, oil (liquid) phase, and gas phase. On the other hand, Titan's fluid will not encounter liquid water until about 100 kilometers under the surface due to the very low temperatures on the surface (Kalousova &

Sotin, 2020). Moreover, interaction between the fluid and water-ice crust result in clathrate hydrate phase in the top few kilometers near the surface (Kalousova & Sotin, 2020), which can also be porous (Genov et al., 2004). The fluids as liquids will migrate until they are contained by alkanotards, which can simply consist of water-ice or clathrate crust with pores that are fully filled with the liquid. Liquids confined in small pores are held tightly by capillary pressure so that effectively block any possible flow across them, unless there is an overpressure from outside the pores. Importantly, there is only a single type of subsurface fluid on Titan, i.e., mixtures of nitrogen and alkanes. The fluid can be in vapor phase only in the vadose zone as the atmosphere penetrates the top crust, but mostly liquid phase in other zones, unless the temperature and pressure are high enough for the fluids to reach supercritical state or vapor-liquid equilibrium as shown later.

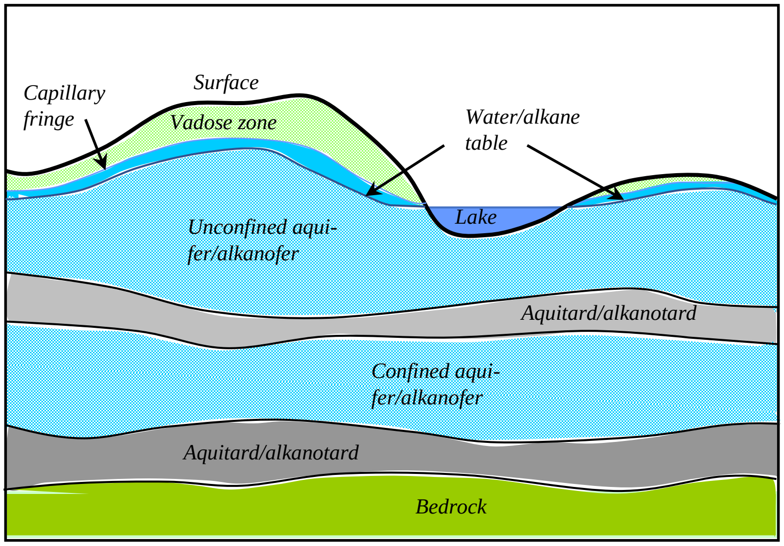

Fig. 1. Analogy of Earth's aquifers and Titan's alkanofers: for Titan, water is replaced with alkane-rich liquid and aquifer/aquitard with alkanofer/alkanotard.

The presence of small pores in crusts makes the porous space available for storing liquids. While the capillaries in Earth's crust may be occupied by both water and hydrocarbons, which make the situation more complicated, those on Titan are occupied by the nitrogen-alkane liquids only. Therefore, the overpressure across the capillaries, which may be provided by the buoyancy due to density difference of hydrocarbon and liquid water on Earth, e.g., in the hydrocarbon migration (England et al., 1987), must be given by the fluid itself on Titan, in addition to the full or partial weight of the overlying crusts if the liquid is in the confined zone. In this sense, Titan's fluids are analogous to both oils in Earth's hydrocarbon reservoirs and water in aquifers. They are made of a single kind of fluid mixture, but with different compositions depending on the location, depth- and latitude-wise according to the vertical temperature gradient and the temperature variation on the surface. Capillary fringes near the water/alkane table may be filled with water on Earth or alkane-rich liquid on Titan due to condensation of the atmosphere that penetrates the vadose zone, but irrelevant in this work as they do not affect the stability of liquid column as discussed later.

3. Titan's surface liquids

For evaluations purposes such as in this work, liquids on Titan's surface may be assumed to consist of three components (Tan & Kargel, 2018), while neglecting trace constituents, and be in vapor-liquid equilibrium (VLE) with the atmosphere with an overall composition of (Tan et al., 2013): 94.3462% nitrogen, 5.65% methane, and 0.0038% ethane. Using PC-SAFT, the composition and density of surface liquids at 94 K and 1.467 bar for low-latitude regions, and 90 K and 1.467 bar for high-latitude regions, are listed in Table 1. The PC-SAFT parameters of all components are taken from Tan & Kargel (2018) along with the associated binary interaction parameters, except for that of nitrogen/ethane, which is set to 0.045 in this work to accommodate the mixture behavior at temperatures in subsurface that is much higher than that on Titan's surface. Consequently, entries in Table 1 may be slightly different from that in our previous works (Tan et al., 2013; 2015). For the record, Cordier et al. (2021) used a value of 0.07 for this binary parameter, which is inaccurate in describing the liquid phase of nitrogen/methane/ethane ternary mixtures in high temperature range of interest as shown in Appendix B.

As seen in Table 1, the composition of the liquids is ethane-rich in low latitudes and methane-rich in high latitudes. Even though the temperature is lower in high latitudes, the liquid density is also lower compared to that in low latitudes due to the more abundant methane (Tan et al., 2015). These surface liquids may come from rainfalls and then flow down to subsurface through large pores and fractures as recharge to the alkanofers. During the flow and after settling down, they are subject to temperature gradient arising from geothermal activities of the moon. Some of the liquids are inevitably trapped in smaller pores, which become smaller with depth due to compaction. However, pores may migrate to warmer location (Smoluchowski & McWilliam, 1984) in water ice, thus in the lower crust due to thermal gradient, so that small pores may still be expected to exist in the deep.

Table 1. Properties of Titan's liquid on the surface in low- and high-latitude regions at atmospheric pressure of 1.467 bar in VLE with the atmosphere

	Surface temperature	Composition (mole%)			Density [kg/m^3]
		Nitrogen	Methane	Ethane	
Low latitudes	94 K	6.97	36.73	56.30	596.08
High latitudes	90 K	20.39	70.04	9.57	544.82

Another possibility is that nitrogen and methane have an endogenic origin so that upward migration from subsurface towards the surface may be expected until reaching a steady state. In this work, the stability of columns in unconfined zone is evaluated at conditions after the steady states are established regardless of either the liquid originates from recharge inflow from precipitation on the surface or outflow of endogenic fluid from the deep. The liquid properties in the column should be the same for both cases as the liquid also maintains equilibrium with the atmosphere on the surface.

4. Modeling methods

4.1. *Equilibrium in gravitational field with heat diffusion*

It has long been known that convection-free fluid columns in a single stable phase α subject to gravity g and a temperature gradient must have conditions according to an extended Gibbs equation (Galliero et al., 2017). The change of chemical potential for each component i of the fluid mixture along the column must be modified by the gravitational potential due to the change of its depth (dh) and its thermal diffusion due to the change of temperature (dT):

$$d\mu_i^{\alpha} = M_i g dh - \frac{Q_i}{T} dT , \qquad i = 1 \ldots N \tag{1}$$

where M_i is the molar mass of component i, g is the gravity (= 1.352 m/s^2 for Titan), T is temperature, Q_i is the heat due to the diffusion of component i, and N is the number of components (N = 3 in this work).

For the thermal diffusion, instead of applying diffusion coefficients, the experimental data of which are scarce at low temperatures, the equation derived from the internal energy is instead used for this work (Firoozabadi et al., 2000):

$$\frac{Q_i}{RT} = -\frac{\overline{U}_i^{\mathrm{R}}}{4RT} + \frac{1}{4RT}\frac{\bar{v}_i}{\sum_j z_j \bar{v}_j}\sum_j z_j \overline{U}_j^{\mathrm{R}} , \qquad i = 1 \ldots N \tag{2}$$

where $\overline{U}_i^{\mathrm{R}}$ and $\bar{v}_i$ are the partial molar residual internal energy and the partial molar volume of component i in the mixture, respectively, which can be calculated using any suitable EOS (see Appendix C). In Eq (2), $\mathbf{z} = \{z_i, i = 1 \ldots N\}$ is the composition and R is the gas constant. This approach was considered more accurate and efficient in a comparison study by Nikpoor et al.

(2013) than two other popular approaches, i.e., Haase’s (1969) and Kemper’s (1989) models. Haase’s approach was applied for Titan’s subsurface liquids in a recent paper (Cordier et al., 2021) while Firoozabadi’s as in Eq (2) was also applied in our presentation (Tan & Kargel, 2020). For interested readers, the comparison between the performances of these two approaches is shown in Appendix B. As mentioned earlier, both works used PC-SAFT as the main EOS, which has been successfully applied for Titan’s fluids (Tan et al., 2013; 2015; Luspay-Kuti et al., 2015; Stevenson et al., 2015; Singh et al., 2017; etc.). The algorithm used for the thermo-gravitational effects in this work is given in Appendix D.

4.2. *Capillary pressure*

Capillary pressure results from the strong adhesive interaction between the solid pore wall and the fluid molecules confined inside the pore. Because of it, the fluid can be condensed as a liquid-like phase and held strongly inside the pore. Only if there is a sufficient overpressure axially across the pore that overcomes the capillary pressure, can the fluid be expulsed and released from the pore. Without the overpressure, the entrapped fluid keeps any potential flows from passing across the porous medium. On Earth, such trapping mechanism occurs with hydrocarbon fluids due to capillary pressure of water confined in small pores of aquitards (England et al., 1987). By analogy, Titan's subsurface liquids are trapped due to the capillary pressure of the liquid in small pores forming an alkanotard.

The pores are commonly modeled as long thin open cylinders with radius r_p, in which the capillary pressure by the wall on the fluid may be calculated using the Young-Laplace (YL) equation:

$$P_\mathrm{cap} = P^\mathrm{L} - P^\mathrm{V} = \frac{2\gamma^\mathrm{LV}}{r_\mathrm{p}} \cos\theta \tag{3}$$

where P^{L} is the pressure of the liquid-like phase inside the pores and P^{V} is the pressure of bulk vapor thermodynamically in equilibrium with the liquid. Note that the calculations of capillary pressure in this model require the assumption of the existence of vapor and liquid in equilibrium but does not necessarily imply an actual phase equilibrium. In Eq (3), the fluid-wall interaction is represented by the surface tension γ^{LV} that separates the liquid from the vapor, which can be calculated using the simple parachor equation (Danesh, 1998):

$$\gamma^{\mathrm{LV}} = \left(\sum_i x_i \wp_i \rho^{\mathrm{L}} - \sum_i y_i \wp_i \rho^{\mathrm{V}} \right)^4 \tag{4}$$

where ρ^{L} and ρ^{V} are the densities of the coexisting phases, i.e., the liquid in the pores and the bulk vapor, respectively. $\wp_i$ is the parachor of component *i* tabulated in Appendix E, while x_i and y_i are the mole fractions of component *i* in the liquid and vapor, respectively.

In small pores of nanometer size, the extreme strength of the fluid-wall interaction is described using a zero contact-angle $\theta = 0$, i.e., the pore wall becomes completely wet, and an effective pore radius r_{e} instead of the physical radius r_{p} (Tan & Piri, 2015):

$$r_{\mathrm{e}} = r_{\mathrm{p}} \left(1 - \lambda(T, r_{\mathrm{p}}) \right) \tag{5}$$

so that the capillary pressure in nanopores is calculated using the modified YL equation:

$$P_{\mathrm{cap}} = \frac{2\gamma^{\mathrm{LV}}}{r_{\mathrm{e}}} \tag{6}$$

The correction parameter λ, which depends on T and r_{p}, can be interpreted as the reduction of pore size due to adsorption layering that precedes the capillary condensation. Because of the lack of experimental data of this layering, λ is commonly derived from experimental capillary-condensation data. For this work, all λ parameters of the individual component of the mixture are given in Appendix E for a typical porous media. For mixtures, the mixing rule for these λ parameters is the simple average $\lambda = \Sigma(x_i \lambda_i)$.

As usual, the vapor-liquid equilibrium for calculating capillary pressure in Eq (6) is carried out using the equality of chemical potentials but with different pressures of the equilibrium phases as expressed in Eq (3) or Eq (6). For further details, the readers are referred to Tan & Piri (2015), which applied PC-SAFT coupled with Eq (6), thus the name PC-SAFT/Laplace EOS. For fluid mixtures in vast amount of porous medium, such as that in subsurface crusts, the phase equilibrium for calculating the capillary pressure occurs at the bubble point as required by material balance (Tan et al., 2019a).

For the record, if the vapor and liquid in the equilibrium are assumed to be an ideal gas and incompressible liquid, respectively, Eq (3) reduces to a well-known approximation, i.e., the Kelvin equation, which was applied by Voss et al. (2007) to describe the capillary effects on Titan's methane liquid. However, both assumptions are inapplicable for Titan's fluids, so that the more general Eq (6) is to be used for more realistic calculations. The assumption of ideal gas has been proven inaccurate by the failure of modified Raoult's law (Tan et al., 2013), while the liquid is undoubtedly compressible as evident in its pressure-dependent densities (Tan et al., 2015).

5. Results and Discussion

With a temperature profile and surface-liquid composition as inputs, the thermo-gravity algorithm described in section 4.1 straightforwardly provides the pressure gradient, density profile, and the corresponding composition grading with depth in unconfined alkanofers, which are in constant communication with the atmosphere above the liquid column.

5.1. Subsurface liquids in unconfined alkanofer

The calculations were first made for two temperature gradients available in the literature (Kalousova & Sotin, 2020) representing two different types of crust, i.e., water-ice crust and methane clathrate crust. For the latter, the case of 15-km thick clathrate crust is used, so that both crusts serve the calculations as the limiting cases for a range of properties resulting from clathrate thickness up to 15 km on top of the water-ice shell. The temperature gradients are for low-latitude regions with a surface temperature of 94 K. Later, for high-latitude regions with a surface temperature of 90 K, the gradients are derived from the low-latitude cases as described in Appendix A. The calculated pressure gradient, density profile, and the composition grading of the subsurface liquid with those thermal gradients are presented in Figs. 2 and 4 for water-ice and methane-clathrate crusts, respectively; both also showing cases in low and high latitudes with properties of surface liquids as listed in Table 1.

As shown in Fig. 2(a), even though the pressure gradients in low and high latitudes are similar to each other, the density behavior is quite different. It decreases monotonically with depth in low latitudes while it increases with depth in the first few kilometers in high latitudes with a maximum at a depth of 7 km before decreasing. As mentioned earlier, such a reverse density profile leads to convective instability as the lighter lower liquids would tend to migrate upward due to buoyancy. This situation is where crust with small pores in the deep can contribute to keep the liquid columns stable. The small pores in the crust can provide the trapped liquid sufficient capillary pressures to seal the space underneath thus blocking the upward convection, so that the crust layer factually acts as an alkanotard. In this case, any bulk liquid below the alkanotard stays in a confined alkanofer, the total pressure of which will increase by a portion or the whole weight of the crust above it, depending on the crustal structure. The analogy with Earth’s hydrocarbon reservoir is almost exact except that the liquid plugging the pores on Earth is usually water.

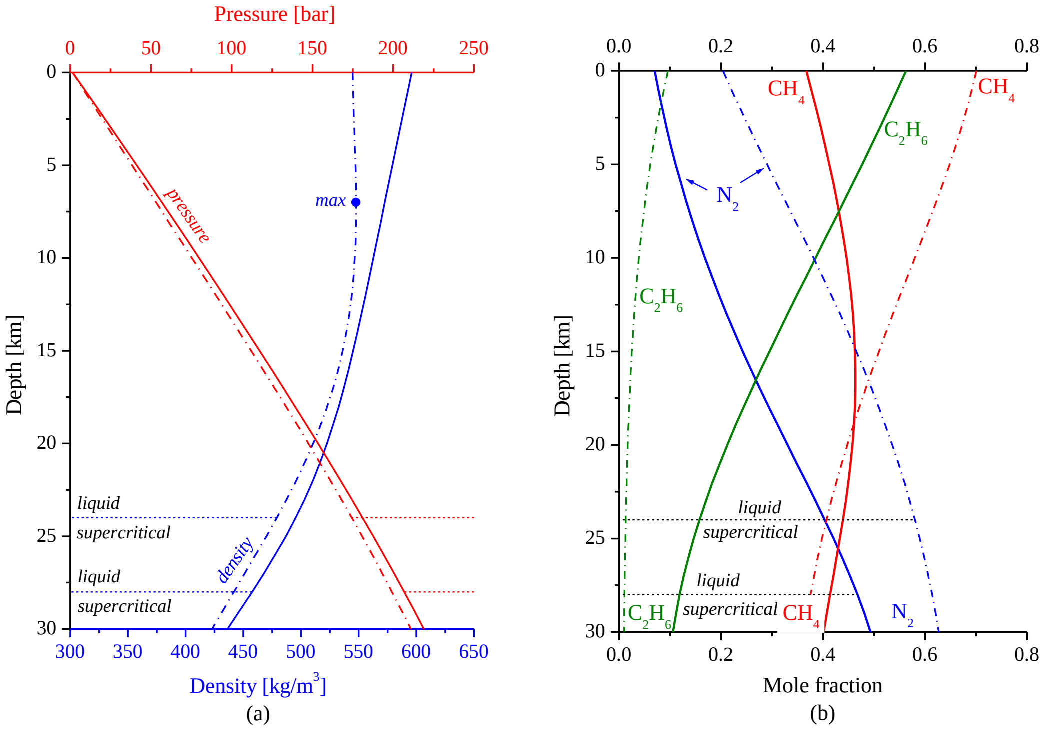

(a)
(b)

Fig. 2. Vertical profiles of subsurface liquid column in water-ice crust: (a) pressure and density; (b) composition. The dash-dotted and solid curves are for high and low latitudes, respectively. The liquid becomes supercritical at the depth of 28 km (low latitudes) and 24 km (high latitudes).

For the composition gradients shown in Fig. 2(b), regardless of the latitudes, the liquids become nitrogen-rich and ethane-lean in the deep when they become supercritical despite their pronounced differences on the surface. Because nitrogen is the most volatile component and ethane is the least volatile component in the mixture, the thermal effect apparently dominates over the gravitational one for Titan’s liquids. The composition grading for high-latitude regions in the first 10 km of depth may be compared with that from Cordier et al. (2021), where the profiles of nitrogen and ethane are similar in both works. However, for methane, it decreases with depth as seen in in Fig. 2(b) while Cordier's is almost constant. For ethane-rich liquid in the low-latitude regions, not discussed in Cordier et al. (2021), methane even increases in the first 10 km.

Another important feature shown in Fig. 2 is the occurrence of supercriticality at the depth of 28 km in low latitudes and 24 km in high latitudes. The pressure-temperature phase diagram corresponding to Fig. 2 is shown in Fig. 3. The supercritical region is at pressures and temperatures above the critical point of the mixture, i.e., the point where the upper dew-point curve meets the bubble-point curve. The shaded area surrounded by dew points is the so-called retrograde region, a well-known phenomenon in oil/gas recovery where the mixture condenses upon depressurizing. In the figure, the dew- and bubble-point curves are calculated at the composition according to the grading with depth. When the liquid becomes supercritical, its properties change dramatically from the original liquid phase, particularly in its ability to effuse porous crust much easier, regardless of the existing pressure. In other words, the fluid can migrate vertically upward easier due to the buoyancy and can later accumulate in an upper space confined by alkanotards, thus resembling oil/gas reservoirs on Earth.

As the pressure builds up, a sufficient overpressure from below may exceed the capillary pressure so that upward leakage may occur across the alkanotard. This seal failure does happen on Earth with hydrocarbon seeps, where oil and natural gas escape the reservoir and flow slowly through network of cracks to the surface (Gluyas & Swarbrick, 2004). All these high-pressure mechanisms might facilitate the slow, continuous supply of methane to Titan’s atmosphere, thus replenishing methane that is destroyed by photolysis. It offers a mechanism alternative to cryovolcanic eruptions (Lopes et al., 2013) as well as outgassing due to the decomposition of methane clathrate hydrates (Choukroun et al, 2010). The latter two mechanisms have long been thought to bring methane and other hydrocarbons from the interior to the surface.

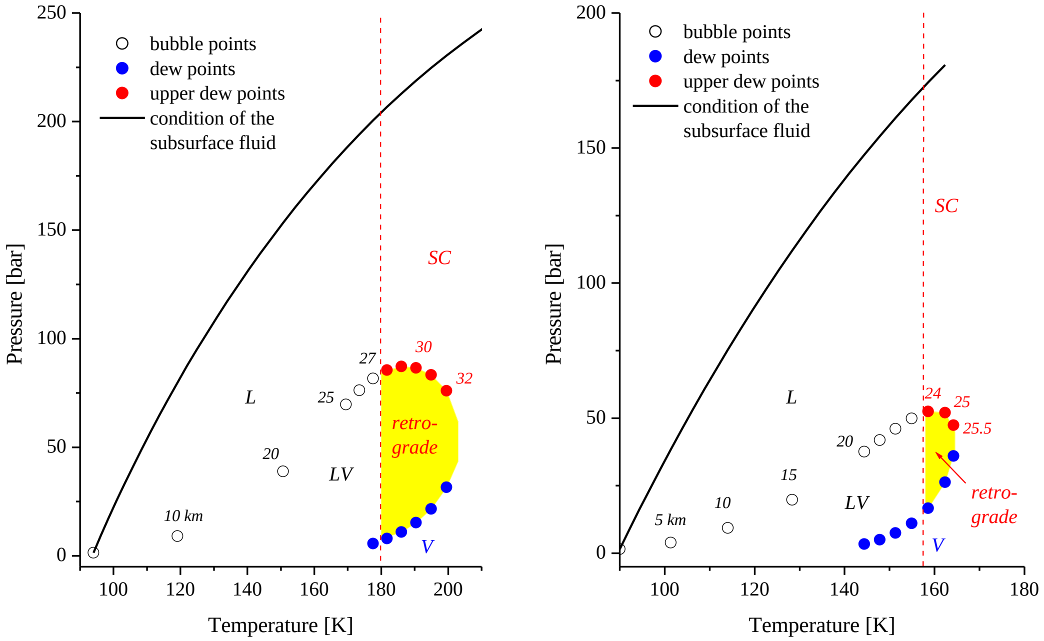

(a)

(b)

Fig. 3. Supercritical region associated with Fig. 2 at: (a) low latitudes; (b) high latitudes. (L = liquid; SC = supercritical; V = vapor; LV = liquid-vapor two-phase region).

For methane-clathrate crusts, the vertical profiles of subsurface liquids are shown in Fig. 4. As the temperature gradient is larger, the liquid density monotonically decreases with depth in all latitudes, and furthermore, if the mixture can stay in deeper location, it even splits into two phases, liquid and vapor, at the depth of 5.64 km in low latitudes and 5.07 km in high latitudes. Consequently, the existing liquid columns are shallower, and the composition grading ends with methane-rich liquid prior to the phase split. Similar to the supercriticality in the previous case, vapor is much more mobile than liquid to migrate upward thus introducing vertical instability to the column. Again, capillaries with entrapped liquid can seal and block the flow, which may eventually lead to accumulation with vapor on top of the liquid if empty space is available below the seal, analogous to gas and oil reservoirs with cap rock on Earth. Another important behavior is that even the ethane-rich surface liquid in the low latitudes quickly becomes ethane-lean not far from the surface (~4 km).

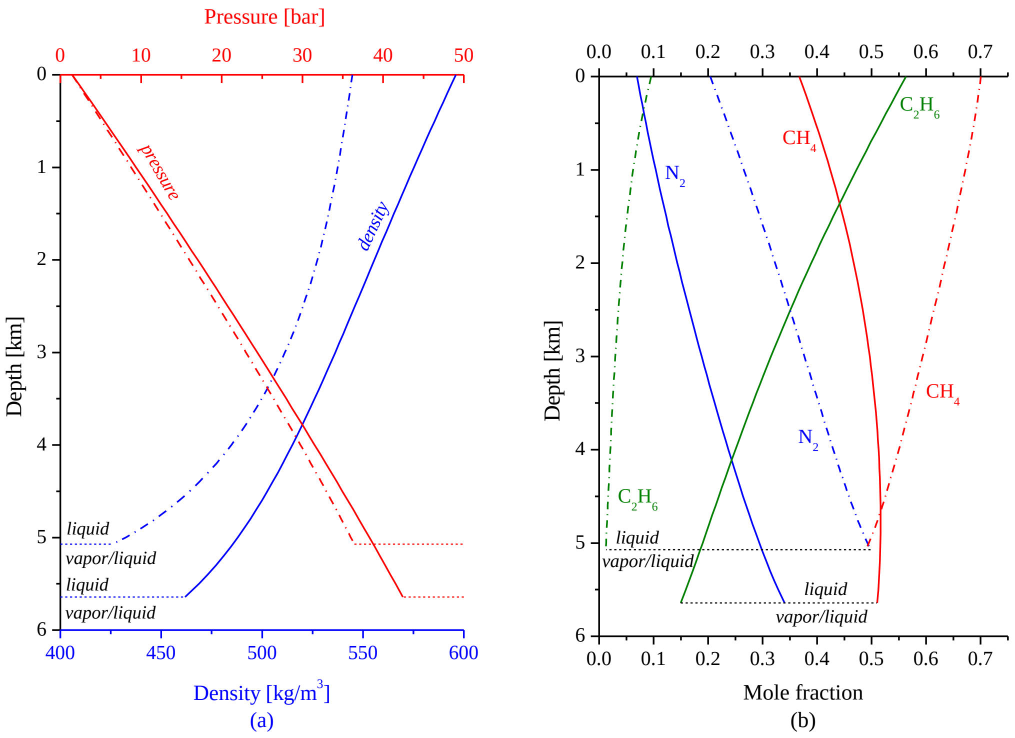

Fig. 4. Vertical profiles of subsurface liquid column in methane-clathrate crust: (a) pressure and density; (b) composition. The dash-dotted and solid curves are for high and low latitudes, respectively. The liquid splits into two phases (in equilibrium with vapor) at the depth of 5.64 km at low latitudes and 5.07 km at high latitudes.

Fig. 5 shows the ternary composition phase diagrams that correspond to the profiles in Fig. 4. The progression of the composition at some depths is plotted as circles in the figure starting from the surface (0 km). The associated phase boundaries at each depth are shown as curves, most of which are bubble-point curves that move faster with depth towards nitrogen-rich region than the composition grading do. This means that the composition is firmly in liquid region in the first few kilometers. However, as the location goes deeper, the bubble-point curves reverse the direction and meet the composition progression at the depth where the phase split into vapor and liquid occurs. For the records, before the reversal, a second liquid appears on the diagram introducing a liquid-liquid and even a three-phase vapor-liquid-liquid region at the methane-lean side of the diagram. For clarity, the three-phase triangular region is only shown in panel (a) for the depth of 2 km and the liquid-liquid regions without three-phase region are only shown in panel (b) for the depths of 0.66 km and 1.95 km. Considering that the composition-grading paths are never even close to liquid-liquid region, let alone the three-phase region, Titan's subsurface liquid will never have a second liquid phase in equilibrium with it. Therefore, any subsurface flow must be in a single phase, i.e., liquid or supercritical, or in two phases vapor and liquid.

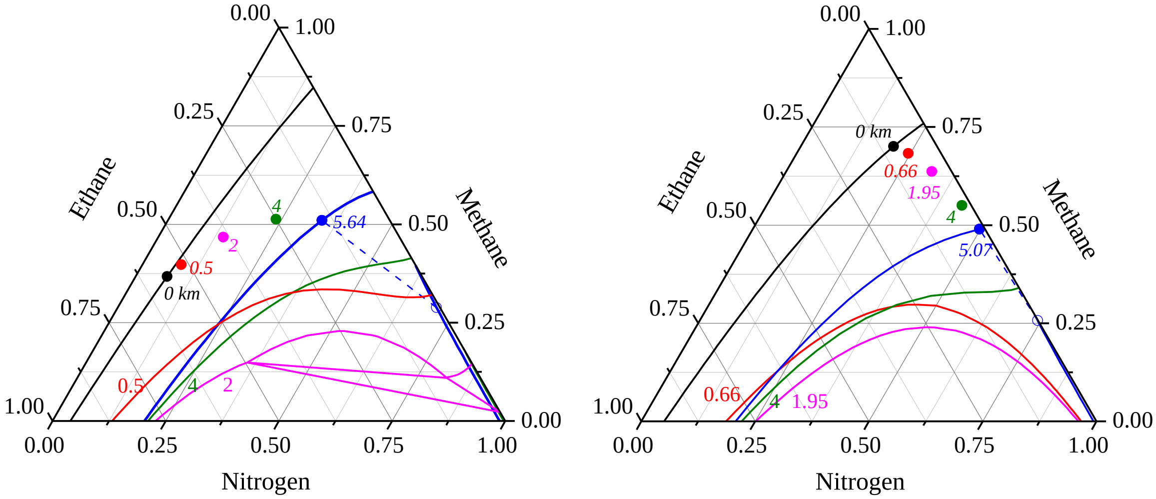

(a)
(b)

Fig. 5. Composition phase diagrams as one descends into methane-clathrate crust from the surface in: (a) low latitudes; (b) high latitudes. Curves: phase boundaries at various depths; points: the corresponding liquid composition due to thermo-gravity effects. Vapor regions are very thin with tiny amounts of ethane. Broken lines: tie lines connecting equilibrium compositions of liquid and vapor. See the text for more details.

Table 2 shows the properties of subsurface liquids at points where bubble or supercriticality is first encountered for all cases discussed above. Upon comparison with the surface conditions in Table 1, the liquid at the phase boundaries is ethane-lean with mole fraction of ethane less than 15 mole%, regardless of the conditions on the surface. Nitrogen is also the dominant component in the liquid, except for the case of methane-clathrate crust in low latitudes, in which methane is dominant. In all cases of water-ice and methane-clathrate crusts, methane is present in substantial fractions in the deep.

Table 2. Properties of Titan's subsurface liquid in low and high latitudes at depths where the liquid is about to bubble or become supercritical

Latitudes	Depth [km]	T [K]	P [bar]	Composition (mole%)*			Density [kg/m^3]*
				N_2	CH_4	C_2H_6	
Methane-clathrate crust: bubble point							
Low	5.64	155.2	42.44	34.02 (70.43)	51.00 (28.82)	14.98 (0.75)	461.8 (138.7)
High	5.07	145.0	36.43	49.82 (74.23)	48.96 (25.70)	1.22 (0.07)	425.9 (134.9)
Water-ice crust: supercritical							
Low	28.0	181.8	206.8	46.76	41.37	11.87	457.7
High	24.0	158.6	174.3	58.02	40.68	1.30	479.1

* The values in parentheses are the properties of vapor in equilibrium with liquid when the first bubbles appear.

For water-ice crust in high latitudes, the density increases with depth in the first 7 km as illustrated in Fig. 2, but then decreases afterwards so that liquids below the depth of 7 km are subject to convection. In fact, there is a maximum temperature gradient that provides monotonically increasing density profile at least until the water-ice crust reaches the bottom of the stagnant lid, below which the crust is no longer conductive. The maximum temperature gradient can be shown using the method in Appendix A to be introduced by a conductive water-ice crust that has a heat flux of q_0 = 3.90 mW/m^2 for low-latitude case, and 6.05 mW/m^2 for high-latitude case, to maintain the stability of liquid columns at least until the bottom of stagnant lid without the assistance of capillary pressure. The values of q_0, however, are much lower than that to produce the 42-km thick stagnant lid, i.e., 13.1 mW/m^2 (Kalousova & Sotin, 2020), and for the low-latitude case it is even less than that due to radiogenic heating, which is 4.35 mW/m^2 on the surface (Fortes, 2012). This contradiction implies that temperature gradients resulting from these values of q_0 cannot be realistic, thus further emphasizing the crucial role of capillary pressures in helping to create the column stability in the subsurface with heat flux much larger than q_0.

5.2. Capillary pressure

As discussed earlier, capillary pressure of liquids confined in small pores may help to maintain the stability of the liquid column if a vertical instability is happening. While pores with radii of 1 – 25 nm can be present in water ice at low temperatures (Raut et al., 2007), pore sizes decrease with depth due to compaction but with an unknown profile. Therefore, a small pore size may be applied to represent pore sizes in large depths as a limiting case. A physical pore radius of 2.2 nm is chosen for calculations in this work due to the availability of reliable experimental data required for the derivation of parameter λ in Eq (5), which are given in Appendix E. For fluid mixtures, as previously pointed out, the capillary pressure is calculated at their bubble points, thus at the same composition as the liquid outside the pores.

In fact, porous mediums statistically exist with pore-size distributions (PSD) from small to large sizes, with the largest ones most susceptible to leakage due to the lowest capillary pressure they can impose on the entrapped liquids. Therefore, for leakage analysis, only the largest pores in the PSD matter. Fig. 6 shows the capillary pressures of liquids trapped inside pores of possible alkanotard with constant radii of 2.2 nm, which may be considered here as the largest pores in the PSD at any depths for the analysis. If the largest pores in the PSD have radii much larger than 2.2 nm and the pore size decreases with depth due to compaction, the capillary pressure is roughly like the dotted curve plotted in Fig. 6 in comparison with the solid curve for the low-latitude case. As pore size decreases with depth, the capillary pressure is lower near the surface and higher in the deep. This dotted curve is for illustration only, not calculated due to the unknown dependency of pore size on pressure/depth. Since the capillary pressure even vanishes in very large pores, where the liquid behaves like in the free bulk, as long as the stability is concerned, liquids confined in larger pores near the surface, such as that in capillary fringes at the bottom of vadose zone, is irrelevant. Even if smaller pores exist in the region, many larger pores or even large fractures are available, thus still allowing migration from underneath to the surface.

The hydrostatic pressure of the liquid column and the lithospheric pressure due to the weight of the crust are also shown in Fig. 6 for comparison. The latter is the maximum value by assuming nonporous crust with a constant density of 934 kg/m^3 for water ice (at 93 K – Lide, 2005) and 890 kg/m^3 for methane clathrate (below 273 K – Makogon, 2010). In fact, the crusts are porous, so their actual density must be lower, regardless of the ability of their pores to store some liquids, which are lighter than the crusts, i.e., less than 600 kg/m^3 as shown by the liquid density in Figs. 2(a) and 4(a). Note that all calculations here are for evaluation purposes, thus providing only rough values to illustrate the order of magnitude of various pressures that can exist in subsurface liquid column. Therefore, it is justifiable here to use the maximum possible lithospheric pressure due to the unknown porosity of the crust.

When liquid is trapped in a confined alkanofer under an alkanotard by capillary pressure, its pressure increases by full lithospheric pressure or just a portion of it. The latter occurs when the crust structure can support some weight of the overlying burden. Without the support, the liquid is “squeezed” by the full burden. This lithospheric pressure can introduce an overpressure from below the alkanotard, but no upward leaks can occur as long as the capillary pressure that seals the alkanotard is higher. Such leaks may potentially occur if the opposing pressures are almost equal in magnitude with slight overpressure. In the situation shown in Fig. 6(a), for example, if an alkanotard of water-ice crust with a largest pore size of 2.2 nm exists at a depth of 14 km in low latitudes (point A), no upward leaks can occur because the lithospheric pressure at this depth (point A') is smaller than the capillary pressure at point A. However, if such an alkanotard exists at a depth of 16 km (point B), upward leaks would occur as the capillary pressure may now be overcome by slight overpressure due to the lithosphere. Thus, the depth of alkanotard that allows such leaks can be as shallow as 11 km (point C) in high latitudes, but deeper at 16 km in low latitudes (point B). In other words, leakage is more likely to occur in high latitudes than low latitudes as the capillary pressure to overcome is lower at the same depth. However, if the largest pore size at a specified depth is larger than 2.2 nm, the capillary pressure is lower and can have values anywhere in the shaded area in Fig. 6(a) in low latitudes. For illustration, as mentioned earlier, it may have a profile such as that shown by the dotted curve in Fig. 6(a), where the depth of the leaks is even shallower at point A' instead of point B. At these locations, a small overpressure from underneath would induce upward leaks. This small overpressure may result from a gradual implosion of the crust structure or additional geothermal activities from the deep that may lead to fluid volume expansion. Once the leaks occur, the escaping fluid becomes liquid phase as the rest of the bulk fluid outside the pores, then subject to the hydrostatic overpressure and the buoyancy due to density difference to flow upward, which are also the major mechanisms of upward migration for oil on Earth. Note that in this case, the liquid has not reached the supercriticality (at depths > 24 km) when the leaks through 2.2-nm pores are allowed to happen at point B or C.

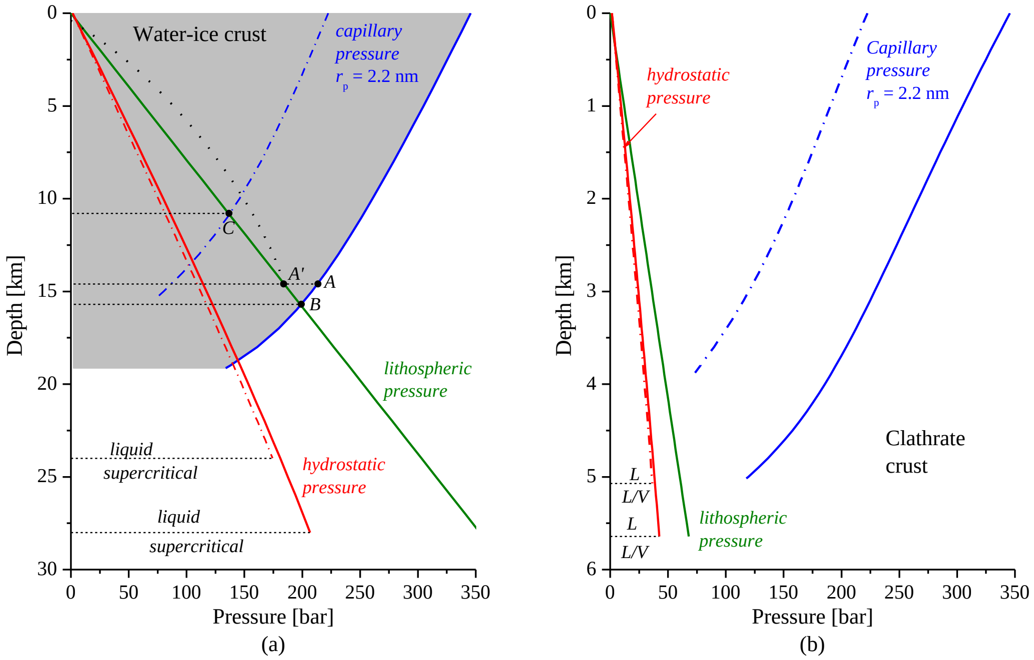

Fig. 6. Capillary pressures of subsurface liquid columns if trapped inside small pores with constant r_p = 2.2 nm in: (a) water-ice crust; (b) methane-clathrate crust. The dash-dotted and solid curves are for high and low latitudes, respectively. Profiles of capillary pressure end when the confined liquid reaches pore critical point in the deep. Read the text for the shaded area and dotted curve in panel (a). Profiles of hydrostatic and lithospheric pressures are also added to the plot for comparison.

In Fig. 6, the profiles of capillary pressure end at the respective pore critical point (Tan et al., 2019b; 2020), where the confined liquid become supercritical, thus introducing a dramatic drop of capillary pressure if not none, which effectively removing the trapping mechanism by the pores. This means, even though the capillary pressures are always higher above the depths of pore critical points in Fig. 6(b), upward migration can still occur at or below the critical-point depths due to the supercriticality in the confinement. Once the leaks occur, the escaping fluid also becomes liquid phase as the rest of the bulk fluid outside the pores and has the same fate as that in the water-ice crust. Note that in this case, the liquid has not reached the depth where the phase split occurs (at depths > 5 km) when the leaks through 2.2-nm pores are allowed due to the supercriticality of the liquids confined in the pores.

6. Conclusions and Remarks

An algorithm for thermo-gravitational effects based on an extended Gibbs equation is applied for calculations on the convection-free pressure/density gradients and composition grading of Titan's unconfined alkanofers in low and high latitudes, for porous water-ice and methane-clathrate crusts. Based on the resulting vertical profiles in both low and high latitudes, upon applying temperature gradients proposed in the literature, the liquid density has reverse profiles where the density decreases with depth, which can introduce vertical convection due to buoyancy, thus instability of the liquid columns. In this case, the stability can be maintained if there are liquids trapped in small pores forming an alkanotard that seals the alkanofer from the top.

Regardless of the conditions of liquid on the surface in different latitudes, the composition of subsurface liquid tends to be nitrogen-rich and ethane-lean in the deep. This behavior indicates that for a liquid column on Titan, the thermal effects dominate over the gravitational counterpart as nitrogen is the most volatile component while ethane is the least volatile, which prefer warmer/deeper and colder/shallower locations, respectively. On the other hand, methane is present in substantial amount in all depths. In the first 10-km depth for water-ice crust at high latitudes, the resulting composition grading is similar to that by Cordier et al. (2021), who applied a different thermo-diffusion model, except for decreasing methane instead of being almost constant.

For Titan's subsurface liquids in water-ice and methane-clathrate crusts, the capillary pressure in alkanotard of the same depth that helps the stability is higher in low latitudes than in high latitudes so that upward leakage is more likely to occur in high latitudes at shallower locations. In any cases of this study, the subsurface liquids can leak upwards before they become supercritical or split into vapor and liquid at deeper locations. When leakage happens, the liquid escapes from the reservoir to the surface, such as that with natural oil seeps on Earth, where oil and natural gas flow slowly through network of cracks to the surface (Gluyas & Swarbrick, 2004). These seeps can be a potential mechanism that spreads widely on the surface and occurs very slowly, which facilitate the need for continuous or episodic supply of methane to Titan's atmosphere to prevent depletion due to photolytic reactions, as an alternative to cryovolcanism (Lopes et al., 2013) and outgassing from dissociation of clathrate hydrates (Choukroun et al., 2010), which have long been thought to bring methane and other hydrocarbons from the interior to the surface. The seeps may also be the source of the extensive wetlands suggested by Neish & Lorenz (2014) in their scenario on the elevation distribution of Titan's craters. Moreover, as found on Earth, hydrocarbon seeps support diverse biological activities (Joye, 2020), thus relevant to research of finding extraterrestrial life.

Author statement

ST: Conceptualization, Methodology, Software, Validation, Formal Analysis, Writing-Original Draft, Writing-Review & Editing.

HA: Conceptualization, Formal Analysis, Writing-Review & Editing.

Declaration of competing interest

The authors declare that they have no known competing financial interests or personal relationships that could have appeared to influence the work reported in this paper.

Acknowledgments

Most of this work was supported by NASA Solar System Workings Grant # 80NSSC19K0792. Only parts with the capillary pressures were done by support from NASA Astrobiology Institute

Grant 17-NAI8_2-0017. ST also thanks Jeffrey Kargel for discussion on thermo-gravity effects in the early stage of the work.

Appendix A. Temperature gradient of conductive crusts

The temperature of subsurface liquids changes according to the temperature profile due to conductive heat flux *q* within the crusts. The crust is assumed to be conductive in transferring heat along the temperature gradient. Therefore, it depends on the properties of the crust material as well as the heat flux *q* available from the deep.

$$\frac{dT}{dh} = -\frac{q}{\kappa(T)} \qquad \text{(A1)}$$

where κ is the thermal conductivity of the crust. For methane-clathrate crust, the thermal conductivity is assumed to be constant at 0.5 W/m/K (Kalousova & Sotin, 2020). Using the constant κ, the gradient in 15-km thick methane-clathrate crust in Kalousova & Sotin (2020) can be calculated with a heat flux of 5.4 mW/m^2. However, for water-ice crust (ice Ih), the conductivity varies with temperature as (based on Ross & Kargel, 1998):

$$\log \kappa(T) = 2.7154 - 0.9752 \log T \qquad [\text{W/m/K}] \qquad \text{(A2)}$$

The assumption of thermal conductive equilibrium heat flux may be valid in shallow crustal depths (upper tens of kilometers), where no solid-state convection is present. This assumption is also valid for literature temperature gradients used in this work (Kalousova & Sotin, 2020) where the solid convection does not happen in the stagnant lid, i.e., until the temperature exceeds 250 K, which is never reached in this work. The bottom of the stagnant lid is 42 km for water-ice crust and 18.5 km for the 15-km thick clathrate crust (Kalousova & Sotin, 2020).

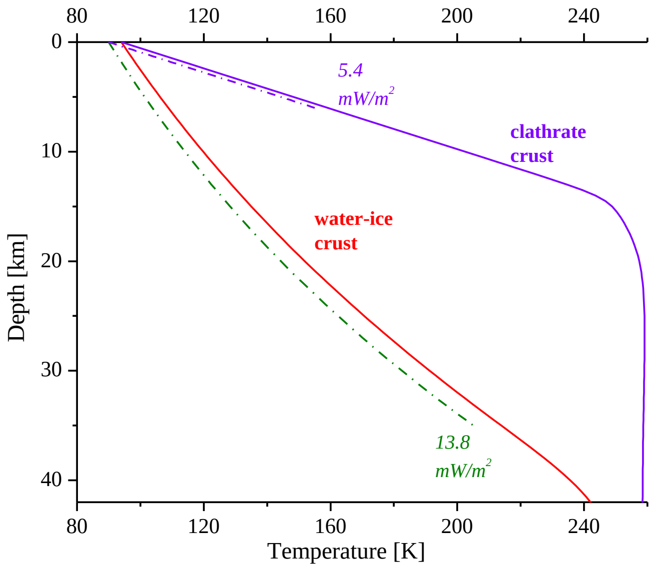

Fig. A1. Subsurface temperature gradients of Titan's crusts in low (solid curves) and high latitudes (dash-dotted curves) applied in this work down to 42 km deep; the gradients in low latitudes are directly taken from Kalousova & Sotin (2020).

Fig. A1 presents all temperature gradients used in this work. Based on Eqs. (A1) and (A2), the temperature gradients in water-ice crust can be calculated. For the gradients in Kalousova & Sotin (2020), the heat is found to be 13.8 mW/m^2, while their heat is slightly smaller at 13.1 mW/m^2, which may be due to different values of heat conductivity was used instead of Eq (A2). However, this difference is not crucial for evaluation purposes in this work. While the temperature gradients in low latitudes in Fig. A1(a) are directly taken from Kalousova & Sotin (2020), the corresponding gradients in high latitudes are calculated using Eqs (A1) and (A2) with q = 13.8 mW/m^2 for water-ice crust, and 5.4 mW/m^2 for methane-clathrate crust.

Appendix B. Effects of using different binary parameters and thermo-diffusion approaches

Fig. A2 shows the performance of PC-SAFT using the binary parameter for N_2/C_2H_6 in this work (0.045), compared to 0.07 that was used by Cordier et al. (2021), to describe the ternary $N_2/CH_4/C_2H_6$ in higher temperature range. As seen in the figures, the smaller binary parameter represents the experimental data (Trappehl & Knapp, 1987) better, particularly obvious in the liquid phase.

The thermo-diffusion approach used in Cordier et al. (2021) is also different from ours as discussed in the paper. Since their surface composition is different from ours, we take the composition of case (b) in Figure 4 of their paper, which is the closest to our case for high-latitude regions, for comparison here. All conditions are first also made the same, including the binary parameter of N_2/C_2H_6 above (0.07), but different approaches of the thermal diffusion. The results are shown in Fig. A3(a), which reveal similar compositional grading within 10 km of depth. While the gradient of C_2H_6 is virtually the same, that of N_2 and CH_4 increase and decrease at larger rates using the current approach, respectively. This discrepancy seems to get larger if the subsurface location is deeper as it is in this work. As discussed in an evaluation by Nikpoor et al. (2013), Firoozabadi's approach that we use is better than Haase's that Cordier et al. used.

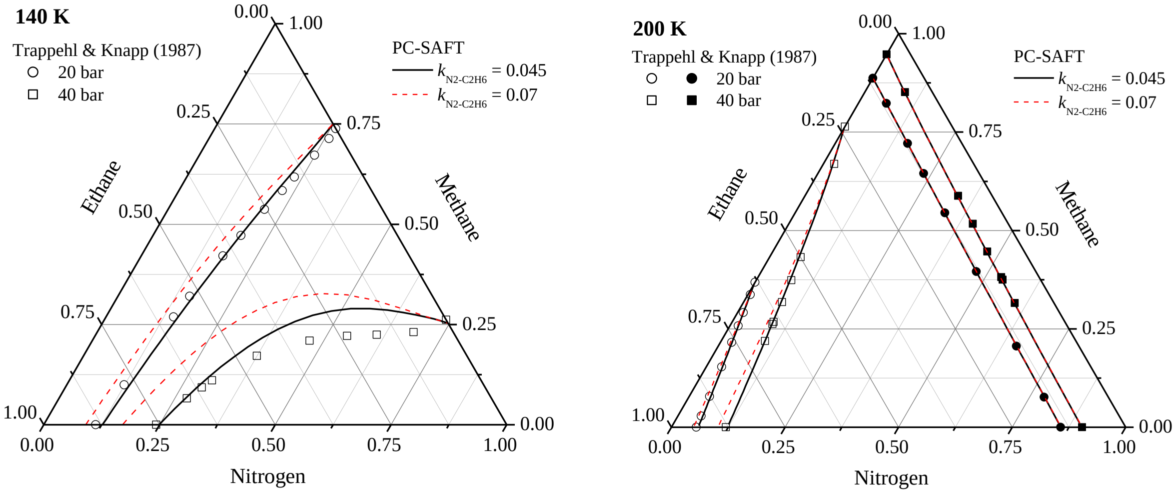

(a)

(b)

Fig. A2. Performance of PC-SAFT for $N_2/CH_4/C_2H_6$ using different binary parameter of N_2/C_2H_6, 0.045 (this work) and 0.07 (Cordier et al., 2021) at: (a) 140 K; (b) 200 K. All other parameters are the same for the comparison. Liquid is near the ethane side while vapor is near the methane side.

To see the discrepancy coming from using both different thermo-diffusion approach and different binary parameter of N_2/C_2H_6, the calculation was repeated, and the results are shown in Fig. A3(b). Obviously, N_2 and C_2H_6 are the components affected by the different parameters. While N_2 is now virtually the same, C_2H_6 decreases at a lower rate for Firoozabadi's thermo-diffusion approach.

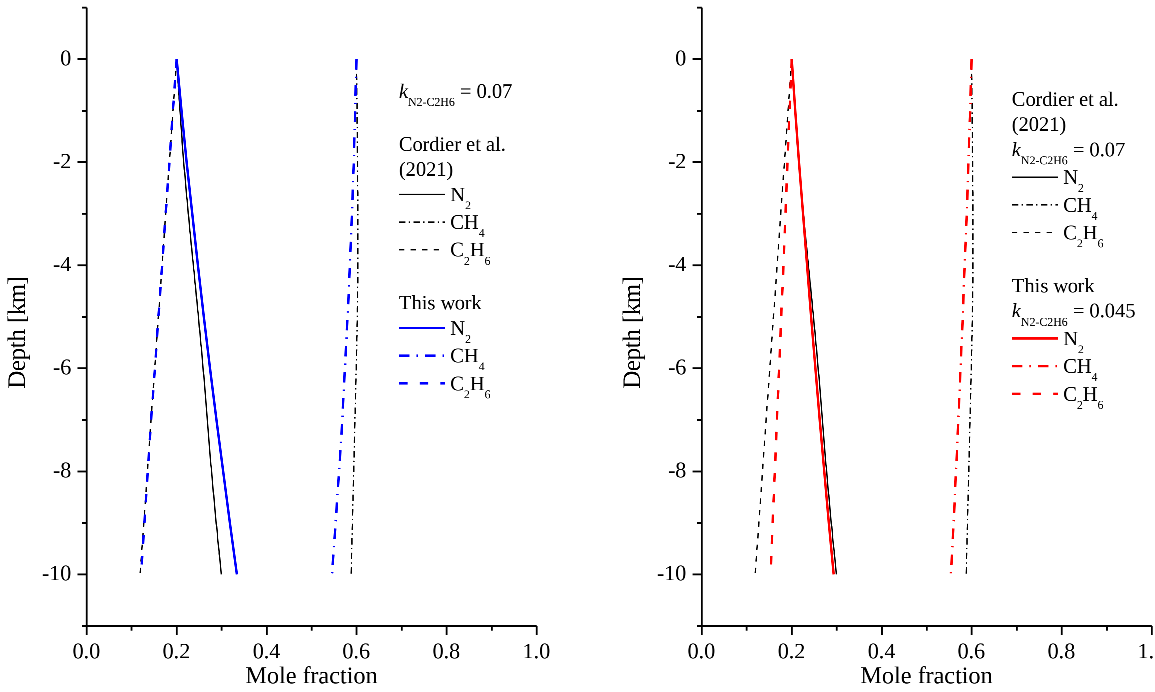

(a) (b)

Fig. A3. (a) Comparison of the results from different thermo-diffusion approach in this work with that in Cordier et al. (2021). The conditions and all parameters are the same for the comparison. (b) Comparison of the results if the binary parameter of N_2/C_2H_6 used in the calculations is also different (0.045 versus 0.07).

Appendix C. Partial molar properties

There are two partial molar properties needed for diffusion-heat calculation in Eq (2), i.e., the partial molar residual internal energy and the partial molar volume of component *i* in the mixture, respectively. They can be calculated by any EOS from the fugacity coefficient of component *i* in the mixture ($\hat{\phi}_i$) through the following expressions.

Partial molar internal energy of component *i*:

$$\bar{U}_i^{\mathrm{R}} = -T\left(\frac{\partial \ln \hat{\phi}_i}{\partial T}\right)_{\rho,\mathbf{z}} - P\left(\frac{\partial \ln \hat{\phi}_i}{\partial P}\right)_{T,\mathbf{z}} \tag{A3}$$

Partial molar volume of component *i*:

$$\frac{\bar{v}_i}{RT} = \left(\frac{\partial \ln \hat{\phi}_i}{\partial P}\right)_{T,\mathbf{z}} + \frac{1}{P} \tag{A4}$$

Appendix D. Algorithm for thermo-gravitational effects

For numerical calculation purposes of pressure gradient and compositional grading, it is useful to slice the liquid into imaginary layers: 1, 2 … *k*-1, *k*, as illustrated in Fig. A4. In this case, Eq. (1) may be formulated for individual layers in terms of fugacity calculated at the average temperature $T(h_{k,k-1})$ estimated at the middle point within the layer $h_{k,k-1} = ½ (h_k + h_{k-1})$. The fugacity of component *i* at *k*-th layer at a depth of $h_k < 0$ can be calculated from the previous (*k*-1)-th layer that is closer to the surface (Galliero et al., 2017):

$$\hat{f}_{i,k}^{\alpha}(T(h_k),\mathbf{z}_k,P_k) = \hat{f}_{i,k-1}^{\alpha}(T(h_{k-1}),\mathbf{z}_{k-1},P_{k-1})\exp\left(\frac{M_i g\Delta h_{k,k-1}}{RT(h_{k,k-1})} - \frac{Q_i}{RT(h_{k,k-1})}\frac{\Delta T_{k,k-1}}{T(h_{k,k-1})}\right) \tag{A5}$$

The computational layer thickness, is the difference between two consecutive depths:

$$\Delta h_{k,k-1} = |h_k - h_{k-1}| \tag{A6}$$

The temperature difference across each layer provided by the temperature profile of the crust is:

$$\Delta T_{k,k-1} = T(h_k) - T(h_{k-1}) \tag{A7}$$

Eq (A3) is solved iteratively from the initial depth at h_0, down to a depth of $h < h_0$. The initial depth h_0 is the surface ($h = 0$) at atmospheric pressure ($P_0 = P_{\text{atm}}$). At a depth h, the temperature is $T(h)$ given by the temperature profile. The outputs of this calculation are the compositional grading and pressure gradient due to the thermo-gravitational effects, and consequently the corresponding liquid density.

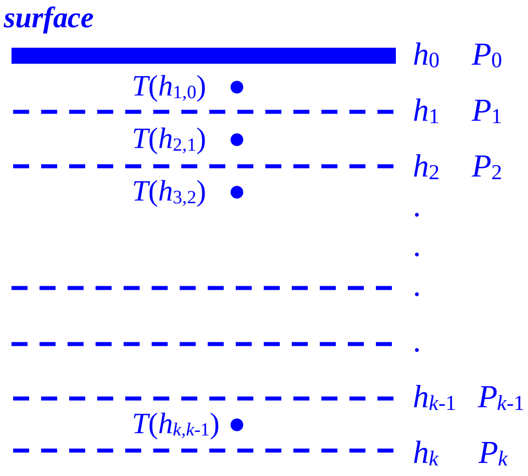

Fig. A4. Intervals of depth, which may be considered as imaginary layers in liquid body for calculations. Note that the average temperature in each layer is taken at the middle of the layer.

The problem in Eq. (A5) has N equations with N unknowns, i.e., the composition $\mathbf{z}_k$ and the pressure P_k for any k-th layer, as also recently pointed out by Baghooee et al (2021). The mole fraction of the last component z_N can be obtained from the fact that $\Sigma z_i = 1$ at any layers. Therefore, this situation is analogous to that for phase-boundary calculations in VLE, i.e., dew point or bubble point. The difference is that Eq (A5) has the exponential as well as different pressures for the fugacities in the *same phase*. However, this difference does not prevent the analogy to be manipulated so that the common phase-boundary algorithm can be readily applied as described below.

As commonly done in phase-boundary calculations, K-values are defined as the ratios of the equilibrium compositions, which are readily adopted for the current extension with thermo-gravitational effect. Because the fluid is in a single phase, i.e., liquid, the compositions for an imaginary layer are the total compositions of the upper ($\mathbf{z}_u$) and the lower ($\mathbf{z}_l$) boundaries of the layer. The K-value of component i are expressed in terms of the fugacity coefficients:

$$K_i = \frac{z_{l,i}}{z_{u,i}} = \frac{\hat{\phi}_i^{\alpha}(T(h_{l,u}), z_u, P_u)}{\hat{\phi}_i^{\alpha}(T(h_{l,u}), z_l, P_l)} \frac{P_u}{P_l} \exp\left(\frac{M_i g \Delta h_{l,u}}{RT(h_{l,u})} - \frac{Q_i}{RT(h_{l,u})} \frac{\Delta T_{l,u}}{T(h_{l,u})} \right) \tag{A8}$$

In solving Eq (A8) with known properties at h_u, the convergence at h_l is reached when all K-values are equal to unity as their analogous counterparts are in phase-boundary calculations. The flow chart in Fig. A5 describes the computation as a root-finding of functions $K_i - z_{l,i}/z_{u,i} = 0$ for all i subject to $\Sigma z_{l,i} - 1 = 0$, which is the routine of calculating dew/bubble points (inside the dashed-line box). Solution using this approach needs only slight changes from the commonly available coding for phase-boundary calculations: instead of using just the ratio of fugacity coefficients as K_i, the ratio of different pressures and the exponential that contains the thermo-gravitational effect must be added, as given in Eq (A8). Moreover, the properties involved in Eq (A8) need their equivalence to be defined for the algorithm as follows.

The pressure at the lower layer P_l is the “phase-boundary” pressure to be calculated together with the corresponding composition $\mathbf{z}_l = \{z_{l,i}\}$ analogous to the composition of the “incipient phase”. The terms in the quotation marks are well defined in the analogous phase-boundary calculation. The lower layer in Eq. (A8) may be arbitrarily labeled as “liquid”, so that the “phase boundary” in the calculation is the “dew point” and the “incipient phase” is “liquid phase”. Of course, the reverse is also equally effective, i.e., if the lower layer is instead labeled as "vapor phase", then the "phase boundary" in the calculation is the "bubble point", so that the "incipient phase" is "vapor phase".

It is worth noting that this algorithm does not specifically depend on the choice of EOS in calculating the fugacity coefficients, nor the fluid mixtures and the planetary bodies. Therefore, they can be considered as independent subroutines that are applicable for describing other fluids on other planetary bodies, even if another accurate EOS is used.

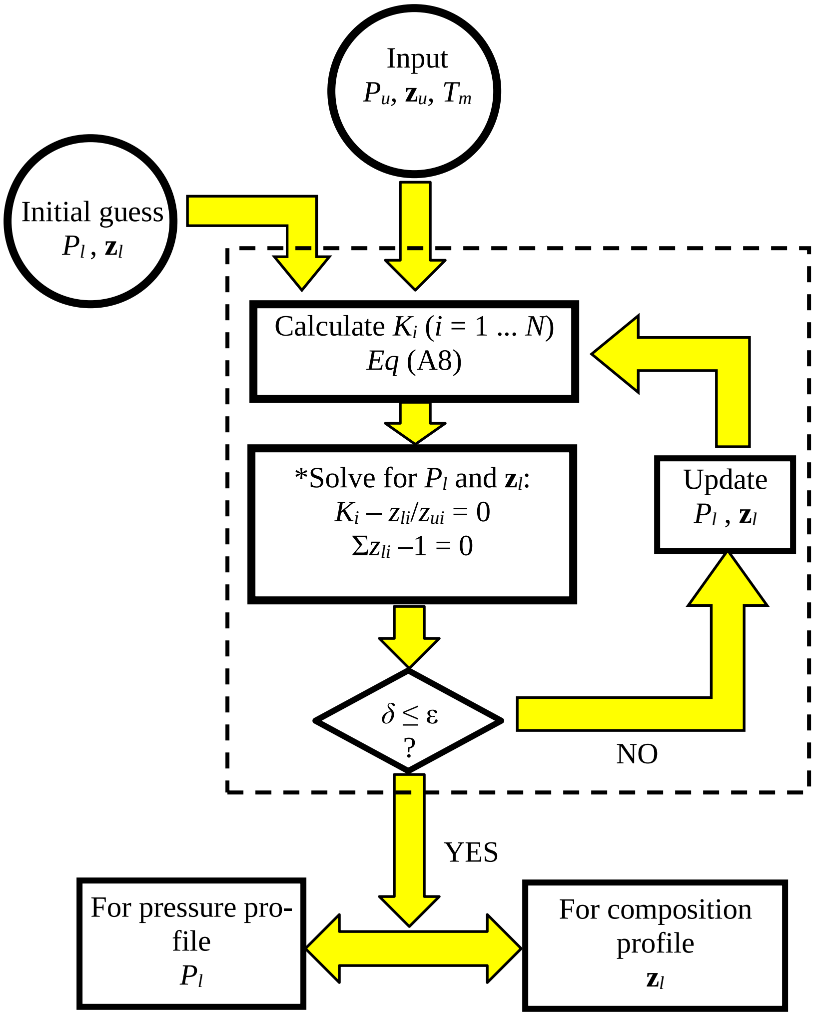

Fig. A5. Flow chart for solving Eq. (A5) using a routine for iterative phase-boundary calculation (inside the dashed-line box). *Newton-Raphson method is used to calculate new values of P_l and

$\mathbf{z}_l$, where δ and ε are the error of the calculation method and a small number, respectively, as the stopping criterion. Initial guesses of a higher pressure than P_u may be used, while that of composition may be made equal to $\mathbf{z}_u$.

Appendix E. Parameters needed for capillary-pressure calculations

The first group of parameters is the parachors for the surface-tension calculations in Eq (4), which can all be derived from literature data of surface tension. The parachors are listed in Table 3. Using these parachors, the calculated surface tension has the unit of mN/m (or dyne/cm) if the densities are in mol/cm^3.

Table 3. Parameters needed for capillary-pressure calculations

Component *i*	$\wp_i$	$T_{\mathrm{C}i}$ [K]	A_i
Nitrogen	60.50	126.192	−1.19024
Methane	71.95	190.564	−1.93301
Ethane	111.0	305.330	−1.14895

The second group is the λ parameters of the individual component of the mixture needed for the effective pore radius in Eq (5). Even though these parameters also depend on the material type of the porous medium, for evaluation purposes in this work that only needs the order of magnitude of the capillary pressure, silica MCM-41 that has effectively uniform pore size is used in this work. MCM-41 is also commonly used in adsorption experiments for investigating confinement effects in engineering disciplines. Furthermore, a pore radius of 2.2 nm is chosen in this work due to the reliability of capillary-condensation data for nitrogen in the literature that can be used as benchmark for deriving the parameters of methane and ethane. The derivation procedure is given in the Supplementary Material, while the resulting parameter for component *i* is in the exponential form:

$$\lambda_i(T) = \exp A_i\left(1 - \frac{T}{T_{\mathrm{C}i}}\right) \tag{A9}$$

where $T_{\mathrm{C}i}$ is the critical temperature of component i, and A_i is the coefficient derived from the experimental capillary-condensation data. Both $T_{\mathrm{C}i}$ and A_i are given in Table 3.

Appendix F. Supplementary Materials

The supplementary file is available online. It contains the numerical values plotted in the figures, the derivation procedure of parameter λ, and the codes of thermo-gravitational routines that can be coupled with an EOS of readers' choice.

References

Baghooee, H., Montel, F., Galliero, G., Yan, W., Shapiro, A., 2021. A new approach to thermal segregation in petroleum reservoirs: Algorithm and case studies. J. Petrol. Sci. Eng. 201, 108367. DOI: 10.1016/j.petrol.2021.108367

Berg, R.R., 1975. Capillary Pressures in Stratigraphic Traps. AAPG Bulletin 59, 939-956. DOI: 10.1306/83D91EF7-16C7-11D7-8645000102C1865D

Brown, R.H., Soderblom, L.A., Soderblom, J.M., Clark, R.N., Jaumann, R., Barnes, J.W., Sotin, C., Buratti, B., Baines, K.H., Nicholson, P.D., 2008. The identification of liquid ethane in Titan's Ontario Lacus. Nature 454, 607-610. DOI: 10.1038/nature07100

Choukroun, M., Grasset, O., Tobie, G., Sotin, C., 2010. Stability of methane clathrate hydrates under pressure: Influence on outgassing processes of methane on Titan. Icarus, 205, 581-593. DOI: 10.1016/j.icarus.2009.08.011

Cordier, D., Bonhommeau, D.A., Vu, T.H., Choukroun, M.; García-Sánchez, F., 2021. Vertical compositional variations of liquid hydrocarbons in Titan's alkanofers. Astron. Astrophys. 653, A80. DOI: 10.1051/0004-6361/202140789

Danesh, A. PVT and phase behaviour of petroleum reservoir fluids. Elsevier, 1998, p. 286. ISBN: 978-0-444-82196-6.

England, W.A., Mackenzie, A.S., Mann, D.M., Quigley, T.M., 1987. The movement and entrapment of petroleum fluids in the subsurface. J. Geol. Soc, 144, 327-347. DOI: 10.1144/gsjgs.144.2.0327

Firoozabadi, A., Ghorayeb, K., Shukla, K., 2000. Theoretical model of thermal diffusion factors in multicomponent mixtures. AIChE J. 46, 892-900. DOI: 10.1002/aic.690460504

Fortes, A.D., 2012. Titan's internal structure and the evolutionary consequences. Planet. Space. Sci. 60, 10-17. DOI: 10.1016/j.pss.2011.04.010

Freeze, R.A., Cherry, J.A., 1979. Groundwater. Prentice-Hall, Englewood Cliffs, N.J. ISBN: 978-0133653120.

Galliero, G., Bataller, H., Bazile, J.P., Croccolo, F., Vermorel, R., Artola, P.A., Rousseau, B., Vesovic, V. and Bou-Ali, M.M., Ortiz de Zárate, J.M., Xu, S., Zhang, K., Montel, F, 2016. Impact of Thermodiffusion on the Initial Vertical Distribution of Species in Hydrocarbon Reservoirs. Microgravity Sci. Technol. 28, 79-86. DOI: 10.1007/s12217-015-9465-6

Galliero, G., Bataller, H., Bazile, J.P., Diaz, J., Croccolo, F., Hoang, H., Vermorel, R., Artola, P.A., Rousseau, B., Vesovic, V. and Bou-Ali, M.M., 2017. Thermodiffusion in multicomponent n-alkane mixtures. npj Microgravity 3, 20. DOI: 10.1038/s41526-017-0026-8

Genov, G., Kuhs, W.F., Staykova, D.K., Goreshnik, E., Salamatin, A.N., 2004. Experimental studies on the formation of porous gas hydrates. Am. Mineral. 89, 1228-1239. DOI: 10.2138/am-2004-8-910

Gluyas, J., Swarbrick, R., 2004. Petroleum Geoscience. Ch. 3. Blackwell Science, Malden, MA. ISBN 978-0-632-03767-4

Gross, J., Sadowski, G., 2001. Perturbed-Chain SAFT: An equation of state based on a perturbation theory for chain molecules. Ind. Eng. Chem. Res. 40, 1244-1260. DOI: 10.1021/ie0003887

Haase, R., 1969. Thermodynamics of Irreversible Processes. Boston, MA: Addison-Wesley, Chapter 4. ISBN: 978-0-201-05735-5.

Hayes, A.G., Lorenz, R.D., Lunine, J.I., 2018. A post-Cassini view of Titan's methane-based hydrologic cycle. Nature Geoscience 11, 306-313. DOI: 10.1038/s41561-018-0103-y

Høier, L., Whitson, C.H., 2000. Compositional Grading – Theory and Practice, in SPE Annual Technical Conference and Exhibition, Dallas, TX, 1-4 October 2000, SPE 63085, Society of Petroleum Engineers. DOI: 10.2118/63085-MS

Joye, S.B., 2020. The geology and biogeochemistry of hydrocarbon seeps. Annu. Rev. Earth Planet. Sci., 48, 205-231. DOI: 10.1146/annurev-earth-063016-020052

Kalousova, K., Sotin, C., 2020. The Insulating Effect of Methane Clathrate Crust on Titan's Thermal Evolution. Geophys. Res. Lett. 47, e2020GL087481. DOI: 10.1029/2020GL087481

Kempers, L.J., 1989. A thermodynamic theory of the Soret effect in a multicomponent liquid. J. Chem. Phys. 90, 6541-6548. DOI: 10.1063/1.456321

Lide, D.R., ed., 2005. CRC Handbook of Chemistry and Physics (86th ed.), Boca Raton (FL): CRC Press.

Lopes, R.M., Kirk, R.L., Mitchell, K.L., LeGall, A., Barnes, J.W., Hayes, A., Kargel, J., Wye, L., Radebaugh, J., Stofan, E.R.; Janssen, M.A., 2013. Cryovolcanism on Titan: New results from Cassini RADAR and VIMS. J. Geophys. Res.: Planets 118, 416-435. DOI:10.1002/jgre.20062

Luspay-Kuti, A., Chevrier, V.F., Cordier, D., Rivera-Valentin, E.G., Singh, S., Wagner, A., Wasiak, F.C., 2015. Experimental constraints on the composition and dynamics of Titan's polar lakes. Earth Planet. Sci. Lett. 410, 75-83. DOI: 10.1016/j.epsl.2014.11.023

Makogon, Y.F., 2010. Natural gas hydrates – A promising source of energy. J. Nat. Gas Sci. Eng. 2, 49-59. DOI: 10.1016/j.jngse.2009.12.004

Mastrogiuseppe, M., Poggiali, V., Hayes, A., Lorentz, R., Lunine, J., Picardi, G., Seu, R., Flamini, E., Mitri, G., Notarnicola, C., Paillou, P., Zebker, H., 2014. The bathymetry of a Titan sea. Geophys. Res. Lett. 41, 1432-1437. DOI: 10.1002/2013GL058618

Mousis, O., Choukroun, M., Lunine, J.I., Sotin, C., 2014. Equilibrium composition between liquid and clathrate reservoirs on Titan. DOI: 10.1016/j.icarus.2014.05.032

Neish, C.D., Lorenz, R.D., 2014. Elevation distribution of Titan’s craters suggests extensive wetlands. Icarus, 228, 27-34. DOI: 10.1016/j.icarus.2013.09.024

Nikpoor, M. H., Kharrat, R., Chen, Z., 2013. A Comparative Study of Compositional Grading Models in Petroleum Reservoirs. Energ. Source Part A 35, 364-369. DOI: 10.1080/15567036.2010.499423

Raut, U., Fama, M., Teolis, B.D., Baragiola, R.A., 2007. Characterization of porosity in vapor-deposited amorphous solid water from methane adsorption. J. Chem. Phys. 127, 204713. DOI: 10.1063/1.2796166

Ross, R.G., Kargel, J.S., 1998. Thermal conductivity of solar system ices, with special reference to Martian polar caps, in Solar System Ices, de Bergh, C., Festou, M., and Schmitt, B. (Eds.), pp. 33-62, Kluwer Academic.

Singh, S., Combe, J.P., Cordier, D., Wagner, A., Chevrier, V.F.; McMahon, Z., 2017. Experimental determination of acetylene and ethylene solubility in liquid methane and ethane: Implications to Titan’s surface. Geochim. Cosmochim. Acta 208, 86-101. DOI: 10.1016/j.gca.2017.03.007

Smoluchowski, R., McWilliam, A., 1984. Structure of Ices on Satellites. Icarus 58, 282-287. DOI: 10.1016/0019-1035(84)90044-7

Stevenson, J.M., Fouad, W.A., Shalloway, D., Usher, D., Lunine, J., Chapman, W.G., Clancy, P., 2015. Solvation of nitrogen compounds in Titan’s seas, precipitates, and atmosphere. Icarus 256, 1-12. DOI: 10.1016/j.icarus.2015.04.019

Tan, S.P., Kargel, J.S., Marion, G.M., 2013. Titan's atmosphere and surface liquid: new calculation using Statistical Associating Fluid Theory. Icarus 227, 53-72. DOI: 10.1016/j.icarus.2012.10.032

Tan, S.P., Kargel, J.S., Jennings, D.E., Mastrogiuseppe, M., Adidharma, H., Marion, G.M., 2015. Titan's liquids: exotic behavior and its implications on global fluid circulation. Icarus 250, 64-75. DOI: 10.1016/j.icarus.2014.11.029

Tan, S.P., Kargel, J.S., 2018. Multiphase-equilibria analysis: Application in modeling the atmospheric and lacustrine chemical systems of Saturn's moon Titan. Fluid Phase Equilib. 458, 153-169. DOI: 10.1016/j.fluid.2017.11.020

Tan, S.P., Kargel, J.S., 2020. Compositional gradient of Titan’s subsurface fluid due to thermo-gravitational effects. AGU Fall Meeting, Abstract #P067-0005. Last accessed on 11/9/2021, https://agu2020fallmeeting-agu.ipostersessions.com/Default.aspx?s=7E-F6-E4-E0-4E-7A-02-B3-31-CF-5D-61-63-38-F1-1E

Tan, S.P., Barsotti, E., Piri, M., 2019a. Application of material balance for the phase transition of fluid mixtures confined in nanopores. Fluid Phase Equilib. 496, 31-41. DOI: 10.1016/j.fluid.2019.05.011

Tan, S.P., Qiu, X., Dejam, M., Adidharma, H., 2019b. Critical point of fluid confined in nanopores: Experimental detection and measurement. J. Phys. Chem. C 123, 9824-9830. DOI: 10.1021/acs.jpcc.9b00299

Tan, S.P., Barsotti, E., Piri, M., 2020. Criticality of Confined Fluids Based on the Tensile Strength of Liquids. Ind. Eng. Chem. Res. 59, 10673-10688. DOI: 10.1021/acs.iecr.0c01848

Tan, S.P., Piri, M., 2015. Equation-of-state modeling of confined-fluid phase equilibria in nanopores. Fluid Phase Equilib. 393, 48-63. DOI: 10.1016/j.fluid.2015.02.028

Trappehl, G., Knapp, H., 1987. Vapour-liquid equilibria in the ternary mixtures N_2-CH_4-C_2H_6 and N_2-C_2H_6-C_3H_8. Cryogenics 27, 696-716. DOI: 10.1016/0011-2275(87)90050-6

Vance, S., Sotin, C., Choukroun, M., Mitchell, K., 2012. Titan’s subsurface alkanology. Lunar Planet. Sci. 43. Abstract #2939.

Voss, L.F., Henson, B.F., Robinson, J.M., 2007. Methane thermodynamics in nanoporous ice: A new methane reservoir on Titan. J. Geophys. Res. 112, E05002. DOI: 10.1029/2006JE002768

Supplementary Materials

On the stability and phase behavior of Titan's subsurface liquid columns

Sugata P. Tan[1]*, Hertanto Adidharma[2]

[1]Planetary Science Institute, Tucson, AZ 85719, USA
[2]Department of Petroleum Engineering, University of Wyoming, Laramie WY 82071, USA

A. Values plotted on the figures in the main paper

Table S1. Values in Figure 2

Fig. 2a				
Depth	Low latitudes		High latitudes	
[km]	P [bar]	ρ [kg/m^3]	P [bar]	ρ [kg/m^3]
0	1.467	596.08	1.467	544.82
1	9.503	592.71	8.835	545.20
2	17.494	589.34	16.210	545.68
3	25.439	585.98	23.591	546.22
4	33.338	582.64	30.979	546.76
5	41.193	579.31	38.374	547.24
6	49.003	575.99	45.776	547.61
7	56.768	572.68	53.181	547.80
8	64.488	569.38	60.587	547.76
9	72.163	566.08	67.990	547.42
10	79.794	562.77	75.387	546.73
11	87.380	559.42	82.772	545.63
12	94.920	556.03	90.139	544.08
13	102.415	552.57	97.481	542.02
14	109.861	549.00	104.792	539.41
15	117.259	545.28	112.064	536.22
16	124.604	541.38	119.289	532.42
17	131.896	537.22	126.458	527.98
18	139.129	532.76	133.562	522.87
19	146.300	527.92	140.593	517.10
20	153.402	522.62	147.541	510.67
21	160.429	516.80	154.398	503.61
22	167.373	510.37	161.156	495.93
23	174.226	503.27	167.806	487.72
24	180.978	495.46	174.341	479.05
25	187.619	486.93	180.757	470.01
26	194.141	477.72	187.049	460.71
27	200.534	467.91	193.214	451.26
28	206.791	457.66	199.251	441.77
29	212.907	447.12	205.159	432.33
30	218.880	436.48	210.941	423.03
31	224.710	425.90	216.599	413.92
32	230.397	415.51	222.134	405.05
33	235.946	405.40	227.552	396.43
34	241.360	395.62	232.855	388.09
35	246.645	386.22	238.047	380.03

Fig. 2b						
Depth	Low latitudes			High latitudes		
[km]	xN2	xCH4	xC2H6	xN2	xCH4	xC2H6
0	0.0697	0.3673	0.5630	0.2039	0.7004	0.0957
1	0.0768	0.3769	0.5463	0.2202	0.6920	0.0878
2	0.0845	0.3863	0.5292	0.2371	0.6825	0.0804
3	0.0927	0.3953	0.5119	0.2544	0.6720	0.0736
4	0.1016	0.4041	0.4943	0.2721	0.6606	0.0672
5	0.1111	0.4124	0.4765	0.2902	0.6484	0.0614
6	0.1212	0.4202	0.4586	0.3084	0.6355	0.0561
7	0.1320	0.4276	0.4404	0.3267	0.6221	0.0512
8	0.1435	0.4344	0.4221	0.3450	0.6083	0.0467
9	0.1556	0.4406	0.4038	0.3632	0.5942	0.0426
10	0.1684	0.4461	0.3854	0.3812	0.5799	0.0389
11	0.1819	0.4510	0.3671	0.3988	0.5656	0.0355
12	0.1961	0.4551	0.3488	0.4161	0.5513	0.0325
13	0.2110	0.4584	0.3306	0.4330	0.5372	0.0298
14	0.2265	0.4609	0.3126	0.4494	0.5233	0.0273
15	0.2426	0.4625	0.2949	0.4653	0.5096	0.0251
16	0.2592	0.4633	0.2774	0.4806	0.4963	0.0231
17	0.2764	0.4632	0.2604	0.4953	0.4834	0.0213
18	0.2940	0.4622	0.2438	0.5094	0.4709	0.0197
19	0.3120	0.4603	0.2277	0.5229	0.4589	0.0182
20	0.3303	0.4575	0.2122	0.5357	0.4474	0.0169
21	0.3487	0.4539	0.1974	0.5479	0.4364	0.0158
22	0.3671	0.4496	0.1833	0.5594	0.4259	0.0147
23	0.3853	0.4446	0.1701	0.5701	0.4160	0.0138
24	0.4033	0.4390	0.1577	0.5802	0.4067	0.0130
25	0.4206	0.4330	0.1464	0.5897	0.3981	0.0123
26	0.4373	0.4266	0.1361	0.5984	0.3899	0.0117
27	0.4530	0.4202	0.1268	0.6065	0.3824	0.0111
28	0.4675	0.4137	0.1187	0.6139	0.3754	0.0106
29	0.4809	0.4075	0.1117	0.6208	0.3690	0.0102
30	0.4930	0.4014	0.1056	0.6271	0.3630	0.0099
31	0.5039	0.3957	0.1004	0.6330	0.3575	0.0096
32	0.5136	0.3904	0.0960	0.6384	0.3523	0.0093
33	0.5223	0.3854	0.0923	0.6434	0.3475	0.0090
34	0.5301	0.3808	0.0891	0.6481	0.3431	0.0088
35	0.5371	0.3764	0.0864	0.6525	0.3389	0.0086

Table S2. Values in Figure 3

Fig. 3a

Low latitudes

	curve	bubble	dew	upper dew
T [K]	P [bar]	BP [bar]	DP [bar]	UDP [bar]
94.0	1.467	1.467		
96.3	9.503			
98.6	17.494			
100.9	25.439			
103.4	33.338			
105.8	41.193			
108.4	49.003			
111.0	56.768			
113.6	64.488			
116.3	72.163			
119.1	79.794	9.097		
122.0	87.380			
124.9	94.920			
127.8	102.415			
130.9	109.861			
134.0	117.259			
137.2	124.604			
140.5	131.896			
143.8	139.129			
147.2	146.300			
150.7	153.402	38.847		
154.3	160.429			
158.0	167.373			
161.7	174.226			
165.5	180.978			
169.4	187.619	69.711		
173.5	194.141	76.199		
177.6	200.534	81.669	5.687	
181.8	206.791		7.920	85.5042
186.1	212.907		11.006	87.2348
190.4	218.880		15.328	86.587
194.9	224.710		21.592	83.2806
199.5	230.397		31.602	76.0347
204.2	235.946			
209.1	241.360			
214.0	246.645			
219.0	251.805			
224.2	256.846			
229.4	261.772			
234.8	266.588			
240.3	271.300			
246.0	275.910			
251.7	280.423			
257.6	284.842			
263.7	289.172			
269.8	293.414			
276.2	297.573			
282.6	301.651			
289.2	305.650			
296.0	309.573			
302.9	313.422			

Fig. 3b

High latitudes

	curve	bubble	dew	upper dew
T [K]	P [bar]	BP [bar]	DP [bar]	UDP [bar]
90.0	1.467	1.467		
92.2	8.835			
94.4	16.210			
96.6	23.591			
99.0	30.979			
101.3	38.374	3.940		
103.8	45.776			
106.3	53.181			
108.8	60.587			
111.4	67.990			
114.1	75.387	9.329		
116.8	82.772			
119.6	90.139			
122.4	97.481			
125.4	104.792			
128.4	112.064	19.805		
131.4	119.289			
134.5	126.458			
137.7	133.562			
141.0	140.593			
144.4	147.541	37.574	3.380	
147.8	154.398	41.865	5.021	
151.3	161.156	46.093	7.437	
154.9	167.806	49.857	11.041	
158.6	174.341		16.620	52.442
162.3	180.757		26.269	52.009
164.3			36.025	47.395

Table S3. Values in Figure 4

Fig. 4a

Depth	Low latitudes		High latitudes	
[km]	P [bar]	ρ [kg/m^3]	P [bar]	ρ [kg/m^3]
0.0	1.467	596.08	1.467	544.82
0.1	2.271	593.94	2.203	544.11
0.2	3.073	591.81	2.938	543.40
0.3	3.871	589.69	3.672	542.69
0.4	4.667	587.59	4.405	541.98
0.5	5.459	585.51	5.137	541.26
0.6	6.249	583.43	5.868	540.54
0.7	7.037	581.38	6.598	539.80
0.8	7.821	579.33	7.327	539.04
0.9	8.603	577.30	8.055	538.27
1.0	9.382	575.28	8.782	537.47
1.1	10.158	573.28	9.508	536.64
1.2	10.931	571.28	10.233	535.77
1.3	11.702	569.30	10.957	534.88
1.4	12.470	567.33	11.679	533.94
1.5	13.236	565.37	12.400	532.97
1.6	13.999	563.41	13.120	531.95
1.7	14.759	561.46	13.838	530.88
1.8	15.516	559.52	14.555	529.77
1.9	16.271	557.59	15.270	528.60
2.0	17.024	555.66	15.984	527.38
2.1	17.773	553.73	16.696	526.10
2.2	18.521	551.80	17.406	524.75
2.3	19.265	549.88	18.115	523.34
2.4	20.007	547.95	18.821	521.86
2.5	20.746	546.02	19.526	520.31
2.6	21.483	544.08	20.228	518.69
2.7	22.217	542.13	20.928	516.98
2.8	22.949	540.18	21.626	515.19
2.9	23.677	538.21	22.321	513.31
3.0	24.404	536.23	23.013	511.33
3.1	25.127	534.23	23.703	509.26
3.2	25.848	532.21	24.390	507.07
3.3	26.566	530.18	25.074	504.78
3.4	27.281	528.11	25.755	502.36
3.5	27.993	526.02	26.432	499.81
3.6	28.703	523.90	27.106	497.12
3.7	29.410	521.74	27.776	494.29
3.8	30.113	519.54	28.442	491.29
3.9	30.814	517.30	29.104	488.11
4.0	31.512	515.01	29.762	484.73
4.1	32.206	512.66	30.415	481.14
4.2	32.898	510.26	31.062	477.31
4.3	33.586	507.79	31.705	473.21
4.4	34.270	505.25	32.341	468.81
4.5	34.951	502.62	32.972	464.06
4.6	35.629	499.90	33.596	458.90
4.7	36.303	497.08	34.212	453.27
4.8	36.973	494.15	34.821	447.07
4.9	37.638	491.09	35.421	440.16
5.0	38.300	487.88	36.010	432.34
5.073			36.434	425.89
5.1	38.957	484.5007		
5.2	39.610	480.9321		
5.3	40.257	477.1395		
5.4	40.899	473.0824		
5.5	41.536	468.7079		
5.643	42.435	461.7514		

Fig. 4b

Depth	Low latitudes			High latitudes		
[km]	xN2	xCH4	xC2H6	xN2	xCH4	xC2H6
0	0.0697	0.3673	0.5630	0.2039	0.7004	0.0957
0.1	0.0728	0.3735	0.5537	0.2102	0.6983	0.0915
0.2	0.0760	0.3797	0.5444	0.2165	0.6960	0.0875
0.3	0.0792	0.3857	0.5351	0.2228	0.6935	0.0838
0.4	0.0826	0.3915	0.5259	0.2290	0.6908	0.0802
0.5	0.0859	0.3973	0.5168	0.2352	0.6879	0.0769
0.6	0.0894	0.4029	0.5077	0.2414	0.6850	0.0737
0.7	0.0929	0.4084	0.4987	0.2475	0.6819	0.0707
0.8	0.0965	0.4138	0.4898	0.2536	0.6787	0.0678
0.9	0.1001	0.4190	0.4809	0.2596	0.6753	0.0651
1.0	0.1038	0.4241	0.4721	0.2656	0.6719	0.0625
1.1	0.1075	0.4290	0.4634	0.2715	0.6685	0.0600
1.2	0.1113	0.4338	0.4548	0.2774	0.6649	0.0577
1.3	0.1152	0.4385	0.4463	0.2832	0.6613	0.0555
1.4	0.1191	0.4430	0.4378	0.2890	0.6576	0.0534
1.5	0.1231	0.4474	0.4295	0.2948	0.6538	0.0514
1.6	0.1271	0.4517	0.4212	0.3005	0.6501	0.0494
1.7	0.1312	0.4558	0.4131	0.3062	0.6462	0.0476
1.8	0.1353	0.4598	0.4050	0.3118	0.6423	0.0458
1.9	0.1394	0.4636	0.3970	0.3174	0.6384	0.0442
2.0	0.1436	0.4673	0.3891	0.3230	0.6345	0.0426
2.1	0.1479	0.4708	0.3813	0.3285	0.6305	0.0410
2.2	0.1522	0.4742	0.3736	0.3339	0.6265	0.0395
2.3	0.1565	0.4775	0.3660	0.3394	0.6225	0.0381
2.4	0.1609	0.4806	0.3585	0.3448	0.6185	0.0368
2.5	0.1653	0.4836	0.3511	0.3502	0.6144	0.0355
2.6	0.1698	0.4864	0.3437	0.3555	0.6103	0.0342
2.7	0.1743	0.4892	0.3365	0.3608	0.6062	0.0330
2.8	0.1789	0.4917	0.3294	0.3661	0.6020	0.0318
2.9	0.1835	0.4942	0.3223	0.3714	0.5979	0.0307
3.0	0.1881	0.4965	0.3153	0.3767	0.5937	0.0296
3.1	0.1928	0.4987	0.3085	0.3819	0.5895	0.0286
3.2	0.1976	0.5008	0.3017	0.3872	0.5852	0.0276
3.3	0.2024	0.5027	0.2950	0.3924	0.5810	0.0266
3.4	0.2072	0.5045	0.2883	0.3977	0.5767	0.0257
3.5	0.2121	0.5062	0.2818	0.4029	0.5723	0.0248
3.6	0.2170	0.5077	0.2753	0.4082	0.5679	0.0239
3.7	0.2220	0.5091	0.2689	0.4135	0.5635	0.0230
3.8	0.2270	0.5104	0.2625	0.4188	0.5590	0.0221
3.9	0.2321	0.5116	0.2562	0.4242	0.5545	0.0213
4.0	0.2373	0.5127	0.2500	0.4296	0.5499	0.0205
4.1	0.2425	0.5136	0.2439	0.4351	0.5452	0.0197
4.2	0.2478	0.5144	0.2378	0.4407	0.5404	0.0189
4.3	0.2532	0.5151	0.2317	0.4464	0.5354	0.0182
4.4	0.2587	0.5156	0.2257	0.4522	0.5304	0.0174
4.5	0.2643	0.5161	0.2197	0.4581	0.5252	0.0167
4.6	0.2699	0.5164	0.2137	0.4643	0.5198	0.0159
4.7	0.2757	0.5165	0.2078	0.4707	0.5142	0.0152
4.8	0.2816	0.5166	0.2018	0.4773	0.5082	0.0144
4.9	0.2877	0.5164	0.1959	0.4844	0.5019	0.0136
5.0	0.2939	0.5162	0.1899	0.4921	0.4951	0.0128
5.073				0.4981	0.4897	0.0122
5.1	0.3003	0.5158	0.1839			
5.2	0.3069	0.5152	0.1779			
5.3	0.3138	0.5144	0.1718			
5.4	0.3210	0.5134	0.1656			
5.5	0.3285	0.5122	0.1592			
5.643	0.3402	0.5100	0.1498			

Table S4. Values in Figure 5a

Fig. 5a

Bubble-point curve

Depth 0 km

xN2	xCH4	xC2H6
0.0396	0.0000	0.9604
0.0405	0.0163	0.9432
0.0426	0.0493	0.9082
0.0448	0.0828	0.8725
0.0471	0.1167	0.8362
0.0497	0.1511	0.7992
0.0524	0.1859	0.7617
0.0553	0.2210	0.7236
0.0585	0.2565	0.6851
0.0619	0.2921	0.6460
0.0655	0.3280	0.6066
0.0693	0.3639	0.5668
0.0734	0.3999	0.5267
0.0777	0.4358	0.4864
0.0824	0.4717	0.4460
0.0872	0.5073	0.4054
0.0924	0.5428	0.3649
0.0978	0.5779	0.3243
0.1035	0.6127	0.2838
0.1095	0.6470	0.2435
0.1158	0.6809	0.2033
0.1223	0.7143	0.1634
0.1292	0.7471	0.1237
0.1363	0.7794	0.0843
0.1437	0.8110	0.0453
0.1514	0.8420	0.0066
0.1527	0.8473	0.0000

Depth 4 km

xN2	xCH4	xC2H6
0.2111	0.0000	0.7889
0.2143	0.0128	0.7729
0.2210	0.0386	0.7403
0.2283	0.0645	0.7071
0.2362	0.0905	0.6732
0.2448	0.1165	0.6386
0.2542	0.1424	0.6034
0.2644	0.1681	0.5674
0.2756	0.1935	0.5309
0.2878	0.2184	0.4938
0.3012	0.2426	0.4562
0.3158	0.2659	0.4183
0.3318	0.2880	0.3802
0.3492	0.3087	0.3421
0.3681	0.3275	0.3044
0.3885	0.3443	0.2672
0.4101	0.3589	0.2310
0.4327	0.3709	0.1963
0.4559	0.3806	0.1635
0.4789	0.3881	0.1330
0.5012	0.3938	0.1050
0.5220	0.3983	0.0797
0.5410	0.4020	0.0570
0.5577	0.4055	0.0368
0.5722	0.4091	0.0187
0.5843	0.4131	0.0026
0.5861	0.4139	0.0000

Depth 0.5 km

xN2	xCH4	xC2H6
0.1318	0.0000	0.8682
0.1362	0.0162	0.8475
0.1458	0.0485	0.8057
0.1563	0.0804	0.7633
0.1679	0.1117	0.7204
0.1807	0.1422	0.6771
0.1949	0.1718	0.6333
0.2106	0.2001	0.5893
0.2282	0.2269	0.5449
0.2478	0.2518	0.5004
0.2698	0.2744	0.4558
0.2945	0.2943	0.4112
0.3224	0.3108	0.3668
0.3537	0.3234	0.3228
0.3888	0.3315	0.2797
0.4272	0.3348	0.2380
0.4675	0.3338	0.1988
0.5072	0.3296	0.1632
0.5436	0.3244	0.1320
0.5751	0.3197	0.1052
0.6013	0.3164	0.0823
0.6229	0.3146	0.0625
0.6406	0.3143	0.0450
0.6553	0.3153	0.0294
0.6675	0.3173	0.0152
0.6776	0.3202	0.0021
0.6792	0.3208	0.0000

Bubble- and dew-point curves

Depth 5.64 km

xN2	xCH4	xC2H6
0.2031	0.0000	0.7969
0.2045	0.0115	0.7839
0.2075	0.0348	0.7577
0.2106	0.0584	0.7310
0.2139	0.0822	0.7039
0.2175	0.1063	0.6762
0.2214	0.1307	0.6479
0.2255	0.1554	0.6190
0.2300	0.1804	0.5896
0.2349	0.2057	0.5594
0.2401	0.2313	0.5286
0.2458	0.2571	0.4972
0.2520	0.2831	0.4650
0.2587	0.3093	0.4320
0.2661	0.3355	0.3984
0.2741	0.3618	0.3641
0.2829	0.3881	0.3291
0.2925	0.4140	0.2934
0.3031	0.4396	0.2573
0.3146	0.4646	0.2208
0.3273	0.4886	0.1841
0.3412	0.5115	0.1474
0.3563	0.5328	0.1109
0.3729	0.5521	0.0750
0.3914	0.5687	0.0399
0.4130	0.5813	0.0057
0.4172	0.5828	0.0000

yN2	yCH4	yC2H6
0.9875	0.0000	0.0125
0.9800	0.0076	0.0125
0.9651	0.0226	0.0123
0.9503	0.0374	0.0122
0.9358	0.0521	0.0121
0.9215	0.0666	0.0120
0.9073	0.0809	0.0118
0.8933	0.0950	0.0117
0.8795	0.1090	0.0115
0.8659	0.1228	0.0113
0.8524	0.1365	0.0112
0.8390	0.1500	0.0110
0.8258	0.1635	0.0108
0.8126	0.1769	0.0105
0.7995	0.1902	0.0103
0.7865	0.2035	0.0100
0.7734	0.2169	0.0097
0.7602	0.2305	0.0094
0.7467	0.2443	0.0090
0.7329	0.2585	0.0086
0.7185	0.2734	0.0081
0.7032	0.2894	0.0074
0.6864	0.3070	0.0066
0.6672	0.3274	0.0055
0.6438	0.3524	0.0038
0.6116	0.3876	0.0008
0.6043	0.3957	0.0000

With three-phase VLL

Depth 2 km

Bubble-point curve (VL1)

xN2	xCH4	xC2H6
0.2275	0.0000	0.7725
0.2348	0.0142	0.7511
0.2507	0.0420	0.7073
0.2687	0.0691	0.6622
0.2894	0.0949	0.6157
0.3135	0.1191	0.5674
0.3421	0.1409	0.5170
0.3561	0.1486	0.4953

Bubble-point curve (VL2)

xN2	xCH4	xC2H6
0.8158	0.1095	0.0746
0.8102	0.1103	0.0796
0.8204	0.1119	0.0677
0.8280	0.1142	0.0578
0.8340	0.1169	0.0492
0.8387	0.1199	0.0414
0.8424	0.1231	0.0344
0.8455	0.1265	0.0280
0.8480	0.1301	0.0219
0.8500	0.1337	0.0162
0.8517	0.1375	0.0109
0.8529	0.1413	0.0057
0.8539	0.1453	0.0008
0.8541	0.1459	0.0000

Liquid-liquid curve

xN2	xCH4	xC2H6
0.3561	0.1486	0.4953
0.3696	0.1629	0.4675
0.3915	0.1824	0.4261
0.4182	0.2008	0.3810
0.4538	0.2172	0.3290
0.5171	0.2284	0.2545
0.5304	0.2284	0.2412
0.5639	0.2233	0.2128
0.5974	0.2182	0.1844
0.6117	0.2142	0.1741
0.6842	0.1859	0.1299
0.7290	0.1629	0.1081
0.7649	0.1421	0.0930
0.7959	0.1227	0.0814
0.8158	0.1095	0.0746

VLL triangle

xN2	xCH4	xC2H6
0.3561	0.1486	0.4953
0.9773	0.0224	0.0003
0.8158	0.1095	0.0746

Table S5. Values in Figure 5b

Fig. 5b

Bubble-point curve

Depth 0 km

xN2	xCH4	xC2H6
0.2406	0.7594	0.0000
0.2366	0.7538	0.0096
0.2288	0.7422	0.0290
0.2211	0.7301	0.0488
0.2134	0.7175	0.0691
0.2060	0.7043	0.0897
0.1987	0.6906	0.1108
0.1915	0.6763	0.1322
0.1846	0.6615	0.1539
0.1778	0.6462	0.1760
0.1712	0.6305	0.1983
0.1648	0.6142	0.2210
0.1586	0.5975	0.2439
0.1526	0.5803	0.2671
0.1467	0.5627	0.2906
0.1411	0.5447	0.3142
0.1356	0.5262	0.3381
0.1304	0.5074	0.3622
0.1253	0.4883	0.3865
0.1203	0.4688	0.4109
0.1156	0.4489	0.4355
0.1110	0.4288	0.4602
0.1066	0.4083	0.4851
0.1023	0.3876	0.5101
0.0982	0.3666	0.5352
0.0943	0.3454	0.5603
0.0905	0.3239	0.5856
0.0868	0.3023	0.6109
0.0833	0.2804	0.6363
0.0800	0.2583	0.6617
0.0767	0.2361	0.6872
0.0736	0.2137	0.7127
0.0707	0.1911	0.7382
0.0678	0.1685	0.7637
0.0651	0.1457	0.7892
0.0625	0.1228	0.8148
0.0600	0.0998	0.8402
0.0576	0.0767	0.8657
0.0553	0.0536	0.8911
0.0531	0.0304	0.9165
0.0510	0.0071	0.9419
0.0504	0.0000	0.9496

Depth 4 km

xN2	xCH4	xC2H6
0.6599	0.3401	0.0000
0.6455	0.3348	0.0197
0.6047	0.3299	0.0654
0.5458	0.3280	0.1262
0.4759	0.3196	0.2045
0.4121	0.2969	0.2910
0.3623	0.2627	0.3751
0.3247	0.2228	0.4524
0.2960	0.1813	0.5227
0.2734	0.1399	0.5867
0.2552	0.0996	0.6453
0.2401	0.0607	0.6992
0.2275	0.0233	0.7493
0.2203	0.0000	0.7797

Bubble- and dew-point curves

Depth 5.07 km

xN2	xCH4	xC2H6
0.5074	0.4926	0.0000
0.4934	0.4877	0.0189
0.4646	0.4765	0.0589
0.4353	0.4622	0.1024
0.4069	0.4441	0.1490
0.3804	0.4221	0.1975
0.3564	0.3968	0.2468
0.3350	0.3690	0.2960
0.3163	0.3395	0.3442
0.2998	0.3090	0.3912
0.2854	0.2780	0.4366
0.2727	0.2469	0.4804
0.2615	0.2159	0.5225
0.2516	0.1854	0.5630
0.2427	0.1553	0.6020
0.2348	0.1257	0.6395
0.2276	0.0967	0.6757
0.2211	0.0682	0.7107
0.2152	0.0404	0.7444
0.2098	0.0131	0.7771
0.2074	0.0000	0.7926

yN2	yCH4	yC2H6
0.7323	0.2677	0.0000
0.7470	0.2519	0.0011
0.7687	0.2288	0.0024
0.7853	0.2115	0.0032
0.7993	0.1970	0.0037
0.8120	0.1839	0.0041
0.8239	0.1716	0.0044
0.8357	0.1596	0.0047
0.8474	0.1477	0.0049
0.8591	0.1357	0.0051
0.8711	0.1236	0.0053
0.8832	0.1114	0.0055
0.8955	0.0989	0.0056
0.9080	0.0863	0.0057
0.9207	0.0735	0.0059
0.9335	0.0605	0.0060
0.9466	0.0473	0.0061
0.9599	0.0339	0.0062
0.9733	0.0204	0.0063
0.9869	0.0067	0.0064
0.9936	0.0000	0.0064

Two liquids (LL curve)

Depth 0.66 km

xN2	xCH4	xC2H6
0.1863	0.0000	0.8137
0.1903	0.0125	0.7972
0.1943	0.0251	0.7806
0.1986	0.0376	0.7638
0.2030	0.0501	0.7469
0.2076	0.0626	0.7299
0.2124	0.0750	0.7126
0.2174	0.0875	0.6952
0.2226	0.0999	0.6775
0.2281	0.1122	0.6597
0.2338	0.1246	0.6416
0.2399	0.1368	0.6233
0.2463	0.1490	0.6047
0.2530	0.1612	0.5858
0.2602	0.1733	0.5665
0.2678	0.1852	0.5469
0.2760	0.1971	0.5269
0.2847	0.2088	0.5064
0.2942	0.2204	0.4854
0.3045	0.2318	0.4637
0.3158	0.2429	0.4413
0.3283	0.2538	0.4180
0.3424	0.2642	0.3934
0.3585	0.2742	0.3673
0.3778	0.2834	0.3389
0.4020	0.2914	0.3066
0.4370	0.2970	0.2660
0.4471	0.2975	0.2554
0.4531	0.2975	0.2494
0.4599	0.2974	0.2427
0.5000	0.2950	0.2050
0.5447	0.2812	0.1742
0.5521	0.2787	0.1692
0.5586	0.2764	0.1651
0.5698	0.2721	0.1581
0.6105	0.2543	0.1353
0.6403	0.2390	0.1207
0.6651	0.2251	0.1098
0.6869	0.2121	0.1010
0.7066	0.1997	0.0937
0.7247	0.1879	0.0874
0.7416	0.1764	0.0820
0.7575	0.1654	0.0771
0.7726	0.1547	0.0728
0.7869	0.1442	0.0688
0.8007	0.1340	0.0653
0.8140	0.1241	0.0620
0.8268	0.1143	0.0590
0.8391	0.1047	0.0562
0.8511	0.0953	0.0536
0.8628	0.0860	0.0512
0.8742	0.0769	0.0489
0.8853	0.0679	0.0468
0.8961	0.0590	0.0449
0.9067	0.0503	0.0430
0.9171	0.0417	0.0412
0.9273	0.0331	0.0396
0.9373	0.0247	0.0380
0.9471	0.0164	0.0365
0.9567	0.0082	0.0351
0.9662	0.0000	0.0338

Depth 1.95 km

xN2	xCH4	xC2H6
0.2516	0.0000	0.7484
0.2566	0.0123	0.7311
0.2618	0.0246	0.7136
0.2672	0.0368	0.6960
0.2729	0.0490	0.6781
0.2788	0.0611	0.6601
0.2849	0.0731	0.6419
0.2914	0.0851	0.6235
0.2982	0.0970	0.6048
0.3054	0.1089	0.5858
0.3130	0.1206	0.5665
0.3210	0.1322	0.5468
0.3296	0.1437	0.5267
0.3388	0.1551	0.5062
0.3487	0.1663	0.4851
0.3594	0.1773	0.4633
0.3712	0.1880	0.4408
0.3843	0.1985	0.4172
0.3990	0.2086	0.3924
0.4160	0.2183	0.3657
0.4365	0.2272	0.3363
0.4631	0.2349	0.3020
0.5068	0.2396	0.2536
0.5245	0.2391	0.2365
0.5493	0.2352	0.2155
0.5741	0.2314	0.1945
0.5928	0.2264	0.1808
0.6418	0.2089	0.1492
0.6736	0.1946	0.1317
0.6993	0.1816	0.1191
0.7216	0.1694	0.1090
0.7415	0.1578	0.1007
0.7598	0.1467	0.0936
0.7767	0.1359	0.0874
0.7926	0.1255	0.0819
0.8077	0.1153	0.0770
0.8220	0.1054	0.0726
0.8357	0.0957	0.0686
0.8489	0.0863	0.0649
0.8615	0.0770	0.0615
0.8738	0.0679	0.0583
0.8857	0.0589	0.0554
0.8972	0.0501	0.0527
0.9084	0.0415	0.0502
0.9193	0.0329	0.0478
0.9299	0.0245	0.0456
0.9403	0.0162	0.0435
0.9505	0.0081	0.0415
0.9604	0.0000	0.0396

Table S6. Values in Figure 6

Fig. 6a

	Low latitudes			High latitudes	
Depth [km]	Lithospheric P [bar]	Hydrostatic P [bar]	Capillary P [bar]	Hydrostatic P [bar]	Capillary P [bar]
0	0.000	1.467	345.580	1.467	222.518
1	12.628	9.503	337.601	8.835	215.784
2	25.255	17.494	329.530	16.210	208.976
3	37.883	25.439	321.366	23.591	202.060
4	50.511	33.338	313.107	30.979	194.994
5	63.138	41.193	304.743	38.374	187.728
6	75.766	49.003	296.265	45.776	180.200
7	88.394	56.768	287.656	53.181	172.333
8	101.021	64.488	278.894	60.587	164.033
9	113.649	72.163	269.950	67.990	155.183
10	126.277	79.794	260.780	75.387	145.634
11	138.904	87.380	251.327	82.772	135.205
12	151.532	94.920	241.506	90.139	123.672
13	164.160	102.415	231.197	97.481	110.781
14	176.788	109.861	220.218	104.792	96.288
15	189.415	117.259	208.296	112.064	80.080
15.384					73.438
16	202.043	124.604	194.996	119.289	
17	214.671	131.896	179.625	126.458	
18	227.298	139.129	161.081	133.562	
19	239.926	146.300	137.732	140.593	
19.143			133.893		
20	252.554	153.402		147.541	
21	265.181	160.429		154.398	
22	277.809	167.373		161.156	
23	290.437	174.226		167.806	
24	303.064	180.978		174.341	
25	315.692	187.619			
26	328.320	194.141			
27	340.947	200.534			
28	353.575	206.791			

Fig. 6b

	Low latitudes			High latitudes	
Depth [km]	Lithospheric P [bar]	Hydrostatic P [bar]	Capillary P [bar]	Hydrostatic P [bar]	Capillary P [bar]
0.00	0.000	1.467	345.580	1.467	222.518
0.10	1.203	2.271	341.385	2.203	219.177
0.20	2.407	3.073	337.210	2.938	215.874
0.30	3.610	3.871	333.064	3.672	212.613
0.40	4.813	4.667	328.948	4.405	209.388
0.50	6.016	5.459	324.862	5.137	206.194
0.60	7.220	6.249	320.804	5.868	203.025
0.70	8.423	7.037	316.775	6.598	199.876
0.80	9.626	7.821	312.775	7.327	196.742
0.90	10.830	8.603	308.801	8.055	193.618
1.00	12.033	9.382	304.854	8.782	190.498
1.10	13.236	10.158	300.933	9.508	187.378
1.20	14.439	10.931	297.035	10.233	184.251
1.30	15.643	11.702	293.161	10.957	181.113
1.40	16.846	12.470	289.308	11.679	177.958
1.50	18.049	13.236	285.475	12.400	174.781
1.60	19.252	13.999	281.660	13.120	171.575
1.70	20.456	14.759	277.861	13.838	168.335
1.80	21.659	15.516	274.076	14.555	165.054
1.90	22.862	16.271	270.302	15.270	161.727
2.00	24.066	17.024	266.538	15.984	158.345
2.10	25.269	17.773	262.780	16.696	154.901
2.20	26.472	18.521	259.024	17.406	151.389
2.30	27.675	19.265	255.269	18.115	147.799
2.40	28.879	20.007	251.510	18.821	144.124
2.50	30.082	20.746	247.743	19.526	140.354
2.60	31.285	21.483	243.963	20.228	136.479
2.70	32.489	22.217	240.166	20.928	132.489
2.80	33.692	22.949	236.347	21.626	128.374
2.90	34.895	23.677	232.499	22.321	124.122
3.00	36.098	24.404	228.616	23.013	119.722
3.10	37.302	25.127	224.690	23.703	115.162
3.20	38.505	25.848	220.713	24.390	110.430
3.30	39.708	26.566	216.675	25.074	105.516
3.40	40.912	27.281	212.567	25.755	100.410
3.50	42.115	27.993	208.375	26.432	95.106
3.60	43.318	28.703	204.087	27.106	89.598
3.70	44.521	29.410	199.686	27.776	83.890
3.80	45.725	30.113	195.156	28.442	77.989
3.879					73.202
3.90	46.928	30.814	190.475	29.104	
4.00	48.131	31.512	185.620	29.762	
4.10	49.334	32.206	180.564	30.415	
4.20	50.538	32.898	175.276	31.062	
4.30	51.741	33.586	169.721	31.705	
4.40	52.944	34.270	163.857	32.341	
4.50	54.148	34.951	157.641	32.972	
4.60	55.351	35.629	151.019	33.596	
4.70	56.554	36.303	143.936	34.212	
4.80	57.757	36.973	136.334	34.821	
4.90	58.961	37.638	128.152	35.421	
5.00	60.164	38.300	119.340	36.010	
5.017			117.777		
5.073				36.434	
5.10	61.367	38.957			
5.20	62.571	39.610			
5.30	63.774	40.257			
5.40	64.977	40.899			
5.50	66.180	41.536			
5.643	67.901	42.435			

Table S7. Values in Figure A1

Fig. A1

	High Latitudes		
q =	13.8	5.4	[mW/m^2]
Depth [km]	T [K]	T [K]	
0	90.00	90.00	
1	92.16	100.84	
2	94.38	111.69	
3	96.64	122.54	
4	98.96	133.39	
5	101.34	144.24	
6	103.77	155.09	
7	106.25		
8	108.80		
9	111.40		
10	114.07		
11	116.79		
12	119.58		
13	122.44		
14	125.36		
15	128.35		
16	131.41		
17	134.54		
18	137.74		
19	141.02		
20	144.37		
21	147.80		
22	151.31		
23	154.91		
24	158.58		
25	162.34		
26	166.19		
27	170.12		
28	174.15		
29	178.27		
30	182.48		
31	186.79		
32	191.20		
33	195.71		
34	200.33		
35	205.05		

B. Derivation procedure of λ parameters

The exponential behavior of parameter λ with temperature as stated in Eq (A9) in the main paper can be traced to the observation over experimentally derived values shown in Fig. S1(a) for various confined fluids in MCM-41 porous medium. Also note that the parameter is unity at the bulk critical temperature. Moreover, the parameter behaves linearly with respect to the reciprocal of pore radius as shown in panel (b), which also include the origin to represent the free bulk phase where the capillary pressure vanishes; the parameter is also zero at the origin as there is no capillary effect in the bulk.

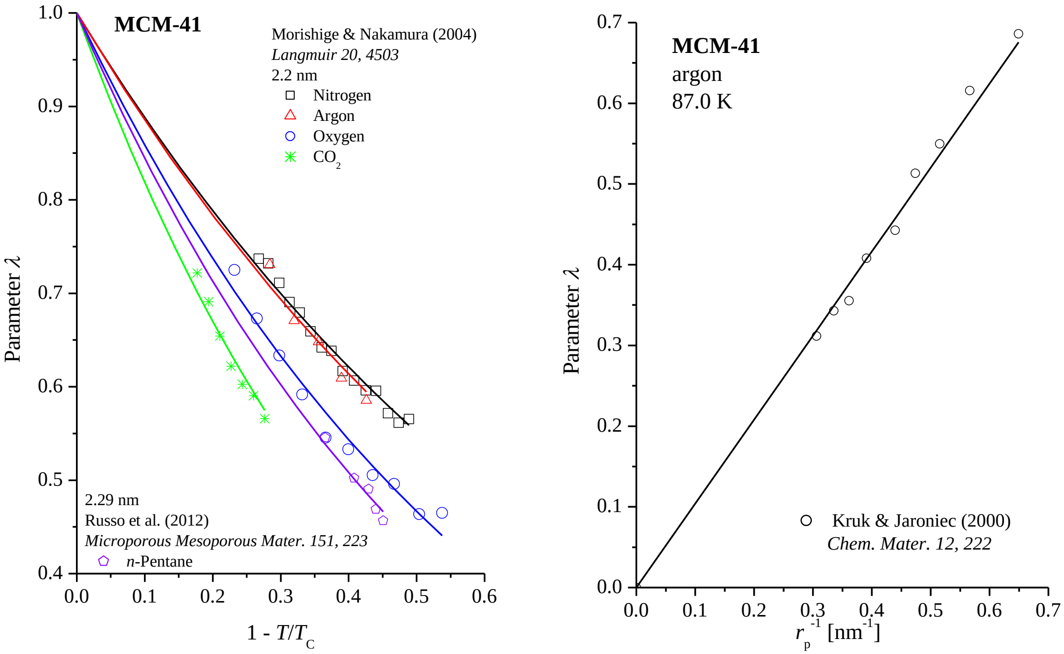

(a) (b)

Figure S1. The behavior of parameter λ from literature with respect to: (a) temperature; (b) pore radius. The parameter's values are derived from experimental capillary-condensation data as in Tan & Piri (Fluid Phase Equilib. 2015, 393, 48).

These behaviors enable us to estimate, to a first approximation, the parameter of a confined fluid as long as there is at least a data value available. We apply the linearity to estimate the parameter if the data is only available for pores of a different but similar size, and then use the exponential to get the coefficient A_i in Eq (A9). For nitrogen, the data in Figure S1 is directly used. However, there is no data for methane and ethane in 2.2-nm MCM-41. Therefore, the estimation as described above is used for these two components. Our measured data of methane at 123.4 K and 126.4 K in 1.77-nm MCM-41 (Yang et al., 2022, Langmuir, accepted), and ethane at pore critical temperature of 225.9 K in 2.1-nm MCM-41 (Tan et al., Ind. Eng. Chem. Res. 2020, 59, 10673) are used for the estimation. For the record, as all data of ethane are supercritical in 2.1-nm MCM-41, the pore critical temperature is calculated by extrapolation down to cross the spinodal. As stated in the main paper, the resulting coefficients A_i are listed in Table 3.

C. Subroutine codes for thermo-gravitational effects

The codes were written in FORTRAN and had been tested and run for the calculations using Compaq Visual Fortran © 2000 Professional Edition 6.6.0. The routines to calculate the fugacity coefficients and density, which depend on the users’ choice of EOS, as well as that calculates the inverse of a matrix, are not included, so they need to be provided by the users.

```
!--------------------------------------------------------------------------------------------
! Program package
! Thermo-gravitational effects: Titan's subsurface liquids
! Written by: Sugata Tan - 2021
! Funded by NASA SSW Grant 80NSSC19K0792
!
! Two subroutines that are equation of state (EOS) specific, to be used with EOS chosen by users,
! are not provided here:
!      (1) DENSITY    -       to calculate the density of a phase at T, P, and composition
!      (2) FCOEF      -       to calculate the fugacity coefficient of a phase at T, P, and
!                                composition
!
! A subroutine to calculate the inverse of an (N x N) matrix is not provided here
!      INVERSE(A,N,D) - to calculate the inverse of matrix A of dimension (N x N); the outputs
!                                are the inverse A and determinant D
!--------------------------------------------------------------------------------------------
! Defining variables universally used across the main program and its subroutines

  MODULE universal_vars

       IMPLICIT NONE
       DOUBLE PRECISION :: P0, dh, dT, grav, R, pi
       DOUBLE PRECISION, DIMENSION(:), ALLOCATABLE :: molWt
       INTEGER :: nComp

  END MODULE universal_vars
!--------------------------------------------------------------------------------------------
! The main program

  PROGRAM Thermograv

       USE universal_vars

       PARAMETER (nC = 3)     ! Titan's fluid is assumed to be a ternary mixture of
                              ! N2(1)/CH4(2)/C2H6(3)
       DOUBLE PRECISION :: MW(nC), Z0_0(nC), Z0_1(nC), Z0_2(nC), Z(nC), X(nC), Y(nC)
       DOUBLE PRECISION :: T0, q, rho
       DOUBLE PRECISION :: h, hmin, hmax, T, TL, TU, P
       INTEGER :: lit, i, n
```

```
       nComp = nC
       ALLOCATE(molWt(nComp))
       R = 83.1447d0         ! Gas constant in [bar.cc/mol/K]

! Titan's fluid; the parameters of pure components depend on the equation of state in use
! (not included here)

       DATA MW /28.018d0, 16.043d0, 30.07d0/        ! The molecular weights of the components:
                                                    ! N2, CH4, C2H6
! The composition at surface in equilibrium with the atmosphere in low latitudes

       DATA Z0_0 /0.069676714d0, 0.367302904d0, 0.563020382d0/

! The composition at surface in equilibrium with the atmosphere in high latitudes

       DATA Z0_1 /0.203892325d0, 0.700433111d0, 0.095674565d0/

! Titan

       grav = 1.352d0        ! [m/s2]       gravity
       P0 = 1.467d0          ! [bar]        pressure at the surface
       molWt = MW            ! molecular weight of the components

! Cases (the value in the last order is the active one for calculation, swap for the desired case)

       lit = 0               ! subsurface liquid in water-ice crust in low latitudes
       lit = 1               ! subsurface liquid in water-ice crust in high latitudes
       lit = 2               ! subsurface liquid in methane-clathrate crust in low latitudes
       lit = 3               ! subsurface liquid in methane-clathrate crust in high latitudes

! Layering

       hmin = 0.d0                  ! from the surface
       dh = -1.d0                   ! [meter]      depth increment set to be 1 meter

       SELECT CASE (lit)

              CASE (0)              ! subsurface liquid in water-ice crust in low latitudes

                     T0 = 94.d0     ! [K]          temperature of surface in low latitudes
                     Z = Z0_0
                     hmax = -3.5d4  ! [meter]      maximum depth of 35 km
                     q = 13.8d-3    ! [W/m2]       heat flux

              CASE (1)              ! subsurface liquid in water-ice crust in high latitudes

                     T0 = 90.d0     ! [K]          temperature of surface in low latitudes
                     Z = Z0_1
                     hmax = -3.5d4  ! [meter]      maximum depth of 35 km
                     q = 13.8d-3    ! [W/m2]       heat flux

              CASE (2)              ! subsurface liquid in CH4-clathrate crust in low latitudes

                     T0 = 94.d0     ! [K]          temperature of surface in low latitudes
                     Z = Z0_0
                     hmax = -6.d3   ! [meter]      maximum depth of 6 km
                     q = 5.425d-3   ! [W/m2]       heat flux

              CASE (3)              ! subsurface liquid in CH4-clathrate in high latitudes

                     T0 = 90.d0     ! [K]          temperature of surface in high latitudes
                     Z = Z0_1
                     hmax = -6.d3   ! [meter]      maximum depth of 6 km
                     q = 5.425d-3   ! [W/m2]       heat flux

       END SELECT

       OPEN(2,file='results.txt')   ! Opening a text file to record the results

! Calculating property profiles of subsurface liquids from hmin to hmax
```

```
       X = Z; Y = Z                  ! Initial guess for the composition at the layer boundaries

       DO h = hmin, hmax, dh

              ht = h+dh/2.d0        ! the middle point of a layer

              ! Temperature profile obtained from Eq (A1)

              IF (lit > 1) THEN      ! methane-clathrate crust
                     T = T0-q*ht/0.5d0
                     TL = T0-q*h/0.5d0
                     TU = T0-q*(h+dh)/0.5d0
                     n = 100
              ELSE                   ! water-ice crust
                     T = (T0**0.0248d0-0.0248d0*ht*q/10.d0**2.7154d0)**(1.d0/0.0248d0)
                     TL = (T0**0.0248d0-0.0248d0*h*q/10.d0**2.7154d0)**(1.d0/0.0248d0)
                     TU = (T0**0.0248d0-0.0248d0*(h+dh)*q/10.d0**2.7154d0)**(1.d0/0.0248d0)
                     n = 1000
              END IF

              ! Calculate the pressure, density, and composition profiles

              dT = TU-TL     ! Temperature increment between lower and upper boundaries of layer

              ! EOS-specific subroutine, using EOS chosen by user, not provided here
              CALL DENSITY(1,P0,T,Z,rho)
              ! Initial value to start the calculation of pressure gradient
              P = P0-rho*sum(z*MW)*grav*dh*1.d-2

              ! Calculate the pressure [bar] and composition Y at the depth of h
              CALL P_COMP(T,P,Z,X,Y)
              ! Calculate the density in [mol/cc] at the depth of h
              CALL DENSITY(1,P,T,Y,rho)
              rho = rho*sum(Y*MW)*1.d3      ! Convert to the unit of [kg/m3]

              ! At this point, X = Z is the composition of the upper boundary and Y is of the
              ! lower boundary of the layer

              ! Print out the results and store in the output file every n meters of depth

              i = INT(h); i = ABS(i)
              IF(MOD(i,n) == (n+INT(dh))) THEN
                      WRITE(2,"(X,F9.2,2(2X,F10.5),3X,3(F15.9,3X),F9.4)") DABS(h+dh), T, P, &
                             &Y(1), Y(2), Y(3), rho
                      PRINT*, DABS(h+dh)    ! For display on screen
              END IF

              ! Updating for the next iteration
              Z = Y
              Y = X
              P0 = P

       END DO
       STOP

END PROGRAM Thermograv

!----------------------------------------------------------------------------------------------
! Subroutine to calculate pressure and composition due to thermo-gravitational effects using the
! algorithm for bubble points at T and Z (see the main paper)

SUBROUTINE P_COMP(T,P,Z,X,Y)

       USE universal_vars

       IMPLICIT NONE
       DOUBLE PRECISION, INTENT(IN) :: T, Z(nComp)
       DOUBLE PRECISION, INTENT(INOUT) :: P, X(nComp),Y(nComp)
       DOUBLE PRECISION :: YY(nComp), K(nComp), KK(nComp), dK_dP(nComp), dK_dY(nComp,nComp)
       DOUBLE PRECISION :: diff, det, delta(nComp+1), func(nComp+1), jac(nComp+1,nComp+1)
       INTEGER :: i, j
```

```
! Newton-Raphson method to solve the phase-equilibrium equations

       diff = 1.d-4; det=1.d0
       X = Z
       DO WHILE (det.gt.1.0D-10)

! Calculate K factors

              CALL KFACT(P,T,X,Y,K)

! Calculate derivative of K factor with respect to composition (mol fraction)

              YY = Y
              DO i = 1,nComp
                     DO j = 1,nComp
                            YY(j)=Y(j)*(1.d0+diff)
                            CALL KFACT(P,T,X,YY,KK)
                            YY=Y
                            dK_dY(i,j) = (KK(i)-K(i))/(diff*Y(j))
                     END DO
              END DO

! Calculate derivative of K factor with respect to P or T

              CALL KFACT(P*(1.d0+diff),T,X,Y,KK)
              dK_dP = (KK-K)/(diff*P)

! The zero functions

              DO i = 1,nComp
                     func(i) = -Y(i)+K(i)*Z(i)     ! energy balance (equifugacity)
              END DO
              func(nComp+1) = -1.d0+SUM(Y)          ! consistency equation

! Build the Jacobian for bubble-point calculations

              DO i = 1,nComp
                     DO j=1,nComp
                            jac(i,j) = Z(i)*dK_dY(i,j)
                     END DO
                     jac(i,i) = jac(i,i)-1.0D0
                     jac(i,nComp+1)=Z(i)*dK_dP(i)
                     jac(nComp+1,i)= 1.d0
              END DO
              jac(nComp+1,nComp+1) = 0.0D0

! Using inverse of Jacobian to solve the linear equations

              CALL INVERSE(jac,nComp+1,det)         ! The INVERSE subroutine is not included

              delta = 0.d0
              DO i = 1,nComp+1
                     DO j = 1,nComp+1
                            delta(i) = delta(i)+jac(i,j)*func(j)
                     END DO
              END DO

              det = 0.d0
              DO i = 1,nComp+1
                     det = det + delta(i)**2
              END DO
              det = DSQRT(det/(nComp+1))

! Updating the variables

              P = P-delta(nComp+1)
              Y = Y-delta(1:nComp)

       END DO

END SUBROUTINE P_COMP
```

```
!-------------------------------------------------------------------------------------------
! Subroutine to calculate the K-factor at P, T, X, Y
! Originally, it is for vapor-liquid equilibria, but now modified for thermo-gravity purposes

SUBROUTINE KFACT(P,T,X,Y,K)

       USE universal_vars

       IMPLICIT NONE
       DOUBLE PRECISION, INTENT(IN) :: P, T, X(nComp), Y(nComp)
       DOUBLE PRECISION, INTENT(OUT) :: K(nComp)
       DOUBLE PRECISION :: ln_fugacityCoef_v(nComp)
       DOUBLE PRECISION :: ln_fugacityCoef_l(nComp), Qnet(nComp)
       INTEGER :: phase

       phase = 1      ! For common vapor-liquid equilibria, change to vapor phase (phase = 0)

! EOS-specific subroutine to calculate phase fugacity coefficient (not provided here)

       CALL FCOEF(phase,P,T,Y,ln_fugacityCoef_v)
       CALL FCOEF(1,P0,T,X,ln_fugacityCoef_l)

! Calculate K-factor

       K = DEXP(ln_fugacityCoef_l-ln_fugacityCoef_v)

! Inclusion of thermo-gravitational effects

       CALL Qdiff(1,P,T,Y,Qnet)      ! Thermal diffusion in subsurface liquid at P, T, Y
       K = K*dexp(-molWt*1.d-2*grav*(dh)/R/T-Qnet/T*dT)*P0/P

END SUBROUTINE KFACT

!-----------------------------------------------------------------------------
! Subroutine to calculate the net heat diffusion in a phase at P, T, X
! Based on Firoozabadi et al. (2000)

SUBROUTINE Qdiff(phase,P,T,X,Qnet)

       USE universal_vars
       IMPLICIT NONE
       DOUBLE PRECISION, INTENT(IN) ::P, T, X(nComp)
       DOUBLE PRECISION, INTENT(OUT) :: Qnet(nComp)
       INTEGER, INTENT(IN) :: phase
       DOUBLE PRECISION :: V(nComp), H(nComp), rho, rho1, rho2, ln_fugacityCoef(nComp)
       DOUBLE PRECISION :: d_lnPhi_dP(nComp), d_lnPhi_dT(nComp), U(nComp)

! Calculate the partial molar volume

       CALL FCOEF(phase,P*1.0001d0,T,X,ln_fugacityCoef)
       CALL FCOEF(phase,P*0.9999d0,T,X,d_lnPhi_dP)
       d_lnPhi_dP = (ln_fugacityCoef-d_lnPhi_dP)/2.d-4/P
       V = (d_lnPhi_dP + 1.d0/P)*R*T
       CALL DENSITY(phase,P,T,X,rho)

! Calculate the partial molar enthalpy

       CALL FCOEF(phase,P,T*1.0001d0,X,ln_fugacityCoef)
       CALL FCOEF(phase,P,T*0.9999d0,X,d_lnPhi_dT)
       d_lnPhi_dT = (ln_fugacityCoef-d_lnPhi_dT)/2.d-4/T
       H = -T*d_lnPhi_dT

! Calculate the partial internal energy

       U = H - P*d_lnPhi_dP

! Calculate the output

       Qnet = (-U+V*sum(X*U)/sum(X*V))/4.d0

END SUBROUTINE Qdiff
```